Structural analysis of gastric H+,K+-ATPase at E1 state using carbon sandwich preparation in cryo-electron microscopy(Dissertation_全文)

AUTHOR(S):

Yang, Fan

Structural analysis of gastric H^+,K^+-ATPase at *E1* state using carbon sandwich preparation in cryo-electron microscopy

Yang Fan

2014 年

Abstract

The gastric proton pump H^+,K^+-ATPase is responsible for the gastric acid secretion, thus also known as a drug target for the treatment of gastric ulcer. Active transport of H^+ and K^+ coupled with ATP-hydrolysis is accomplished by cyclical conformational changes between two principal reaction states (*E1*, *E2*) and their corresponding auto-phosphorylated form (*E1*P, *E2*P). In this study, for better understanding of active transport mechanism by H^+,K^+-ATPase, which exceptionally generates more than a million-fold proton gradient across the membrane, we have attempted to analyzed its structure at *E1* state by electron crystallography of 2D crystals.

In the sample preparation for cryo-EM, we found that by using carbon sandwich preparation in which the crystal solutions are sandwiched between two carbon films, rapid dehydration was prevented and the crystal qualities were preserved, resulting in much better image qualities with improved resolution than those in the ordinary single carbon preparations. This preservation effect was especially important for 2D crystals of membrane proteins with large hydrophilic regions, such as H^+,K^+-ATPase. Together with its prevention of beam-induced image shift, the carbon sandwich preparation is demonstrated to be an efficient and high quality data collection for membrane protein structure analysis, compared with the single carbon preparation.

Applying the carbon sandwich preparation for the 2D crystals of H^+,K^+-ATPase at *E1* state allows us to determine its first 3D structure analyzed at 14 Å. Different from the widely opened N domain found in X-ray structure of SERCA *E1* state, the conformation of the cytoplasmic domains, especially P and N domains, showed compact configuration found in the EM map of H^+,K^+-ATPase *E1* state. This structural evidence was also confirmed by FITC fluorescence study which suggests hydrophobic environment of ATP-binding site at the N domain of H^+,K^+-ATPase *E1* state, most likely due to a close proximity between the N and P domains. Accordingly, close orientation between ATP-binding site (N domain) and auto-phosphorylation site (P domain) of H^+,K^+-ATPase *E1* state might be helpful for the high-affinity ATP binding and subsequent phosphate transfer to the P domain, providing an advantage on the efficient turnover of the vectorial cation transport achieved by H^+,K^+-ATPase, and probably P-type ATPase in general.

Contents

Abbreviations

Å Ångstrom (10^{-10} m)
ABC ATP-binding cassette
ADP adenosine 5'-diphosphate
ATP adenosine 5'-triphosphate
bR bacteriorhodopsin
BAPNA N_{α}-benzoyl-L-arginine-*p*-nitranilide
BSA Bovine Serum albumin
Ca^{2+}-ATPase calcium ATPase
CBB Coomassie brilliant blue
Cryo-EM cryo-electron microscope
CTF contrast transfer function
DOSM dioleoyl sphingomyelin
DTT dithiothreitol
EGTA Ethylenebis(oxyethylenenitrilo)tetraacetic acid
FITC fluorescein 5'-isothiocyanate
FFT Fast Fourier Transform
HCl hydronium chloride
HEPES 2-[4-(2-Hydroxyethyl)-1-piperazinyl]ethanesulfonic acid
H^+,K^+-ATPase proton potassium ATPase
LPR lipid to protein ratio
MES 2-(N-morpholino)ethanesulfonic acid
NaCl sodium chloride
Na^+,K^+-ATPase sodium potassium ATPase
NMR nuclear magnetic resonance
OG n-Octyl-β-glucopyranoside
P-CABs potassium-competitive acid blockers
pH negative decadal logarithmic hydronium
PIPES Piperazine-1,4-bis(2-ethanesulfonic acid)
PLB phospholamban
*p*NPP *p*-nitrophenyl phosphate
PPI proton pump inhibitor
SDS sodium dodecyl sulfate
SDS-PAGE SDS-polyaclylamide gel electrophoresis
SERCA sarco(endo)plasmic reticulum Ca^{2+}-ATPase
Tris tris(hydroxymethyl)aminomethane
2D two-dimensional
3D three-dimensional

CHAPTER 1

General introduction

1.1. P-type ATPase

1.1.1. P-type ATPase superfamily

P-type ATPases —the ion pumping enzyme coupled with ATP hydrolysis— make up a huge superfamily of ion pumps that use the energy of ATP hydrolysis to fuel the transport of charged substrates across biological membranes [Skou, 1957; Axelsen and Palmgren, 1998; Møller *et al.*, 1996]. During this process, an aspartic acid residue in the invariant sequence D*KTG is reversibly phosphorylated to form acyl-phosphate intermediate in which γ-phosphate of the enzymatically hydrolyzed ATP is covalently linked to the Asp side chain [Post and Kume, 1973]; This is a hallmark of more than 300 members of this family that distinguishes "P"-type ATPase from other ATPases, including ABC transporters [Jones and George, 2000; Chang and Roth, 2001], vacuolar type (V-type ATPase) and F_0F_1-ATPases [Nishi and Forgac, 2002; Yasuda *et al.*, 1998; Abrahams *et al.*, 1994]. They translocate a variety of charged substrates including cations, heavy metals and phospholipids across cellular membranes, resulting in a crucial electro-chemical gradient, which is important for many cellular functions in all kingdom of life (eukaryotic, bacterial and archeal) [Bublitz *et al.*, 2011].

It is not easy to describe the structural organization of a "typical" P-type ATPase as there are considerable differences among the members of this family. Some of the P-type ATPases function as two- or multi-subunit complexes, but others seem to work well employing just a single subunit. Several regions of high homology however have been revealed in the structure of the large catalytic subunit; these include phosphorylation site (D*KTG), the KGAP motif in the ATP-binding domain, and the TGES motif located in an extracellular loop which is involved in dephosphorylation step (Fig.1.1).

Based on the type of transported cations (heavy-metal or non-heavy-metal), structural features and molecular evolution, P-type ATPases are classified into five distinguished groups (Fig 1.2): bacterial K^+-transporting, multi-subunit complex (Type P1A, KdpFABC) [Epstein and Kim, 1971], those that transport heavy metals such as Cu^{2+}, Cd^{2+} and Hg^{2+} (Type P1B) [Argüello *et al.*, 2007], the plant and fungal H^+-ATPases (Type P3) [Auer *et al.*, 1998], transport hydrophobic substances (Type P4) [Puts and Holthuis, 2009; López-Marqués *et al.*, 2011], recently identified group whose transport substrate has been elusive (Type P5) [Axelsen and Palmgren, 1998; Sørensen *et al.*, 2010] and the best-studied Type P2 group including Ca^{2+}-ATPase, Na^+,K^+-ATPase and *gastric H^+,K^+-ATPase* (the subject of this study). Sarco(endo)plasmic reticulum Ca^{2+}-ATPase (SERCA), the plasma membrane, and the secretory pathway are vital for muscle function, Ca^{2+} signaling and Ca^{2+} transport into secretory vesicles. The Na^+,K^+-ATPase maintain the essential plasma membrane potential in eukaryotic cells, which provides energy for central cellular processes like the secondary transport of metabolites and the basis for electrical excitation in neurons. The gastric H^+,K^+-ATPase is responsible for the acidic environment of the stomach lumen [Kühlbrandt, 2004; Palmgren and Nissen, 2010].

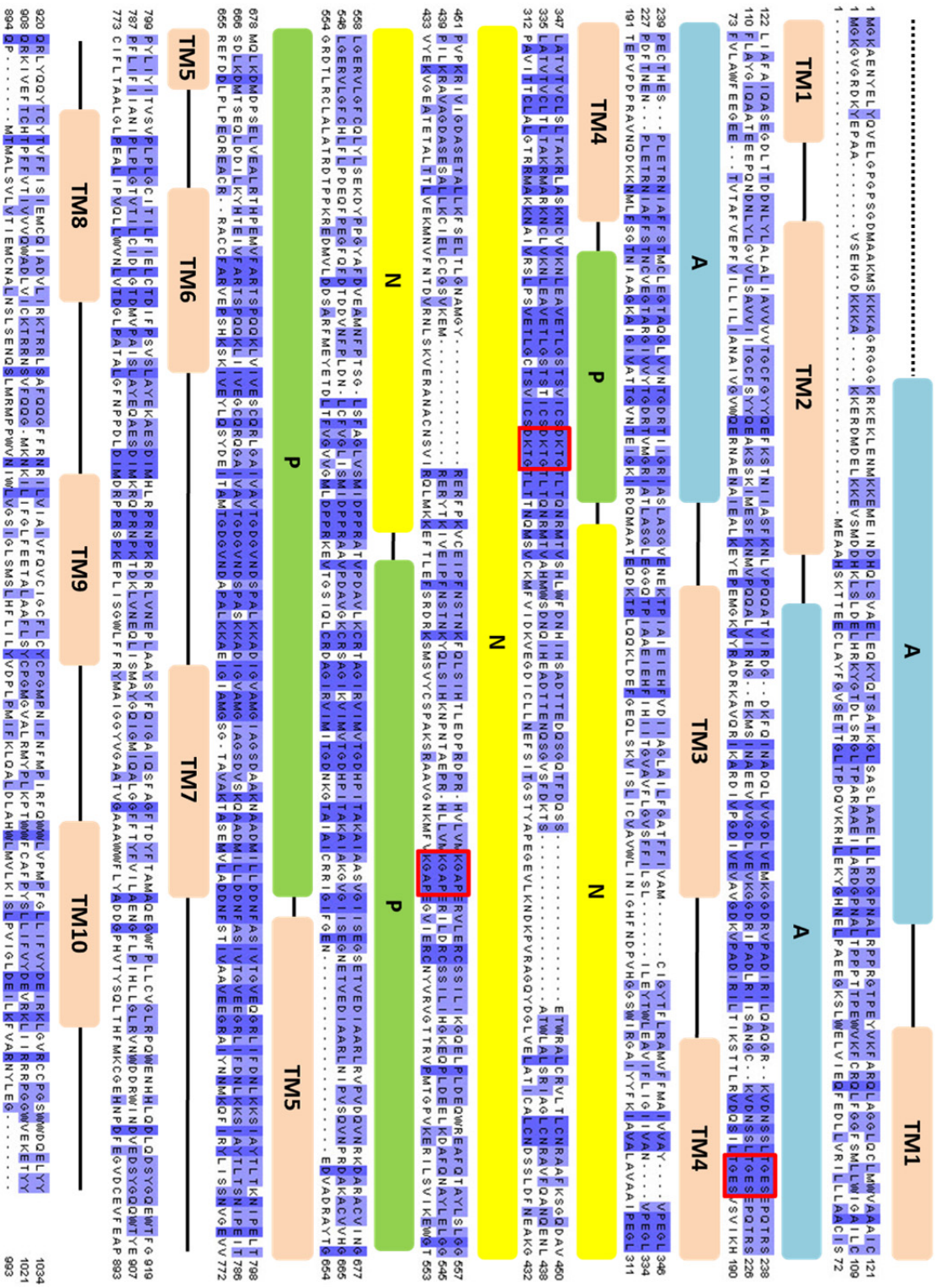

Fig. 1.1. Sequence alignment

Protein sequence alignment of pig gastric H^+,K^+-ATPase (lane 1) with pig Na^+,K^+-ATPase (lane 2) and rabbit SERCA (lane 3). Same color representing similar or same sequence. Dot line represents no corresponding amino acids for the other protein sequences. Conserved TGES motif in A domain (blue boxes), DKTG motif in P domain (green boxes) and KGDP in N domain (yellow boxes) are marked in red boxes. Wheat boxes indicate regions responsible for transmembrane helices.

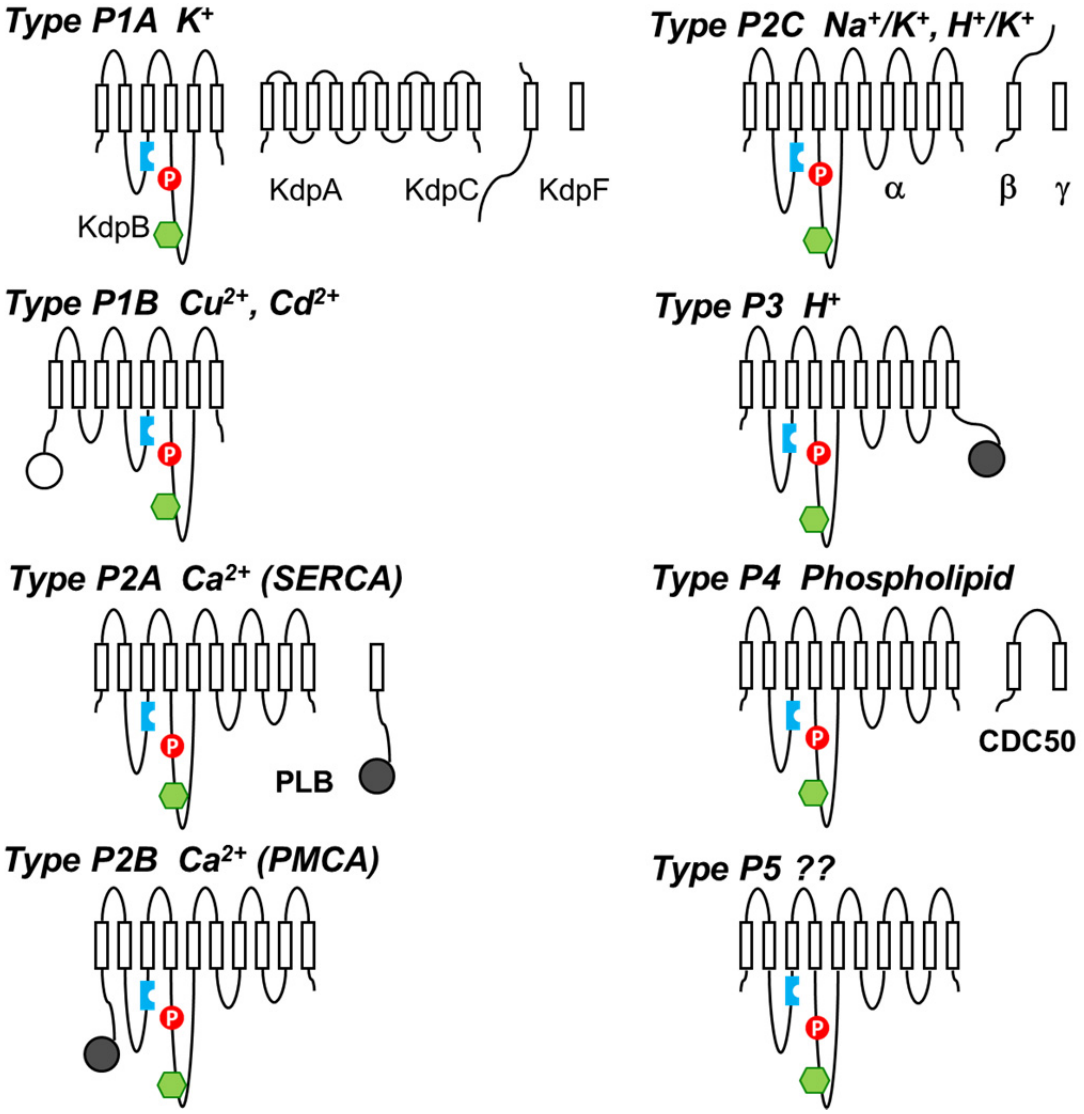

Fig. 1.2. Overview of P-type ATPases

Families are designated by Arabic numbers followed by the transport substrates. Open boxes indicate transmembrane segments: blue boxes, TGES motif; red "P" circle, invariant DKTG phosphorylation site; green hexagons, KGAP ATP-binding motif; open circles, heavy-metal binding motif; closed circles, auto-inhibition domain. K^+-channel-like KdpA subunit is responsible for the K^+-permeation in Type P1A Kdp-ATPase. Phospholamban (PLB) and β, γ-subunit so far have been only shown to be SERCA and Na^+,K^+-ATPase isozyme, respectively, although H^+,K^+-ATPase requires only β-subunit along with the catalytic α-subunit. CDC50 is a regulatory subunit for P4-type ATPase whose structure and function is substantially overlapped with that of β-subunit. There has been no assignment of ligand specificity for P5-type ATPases.

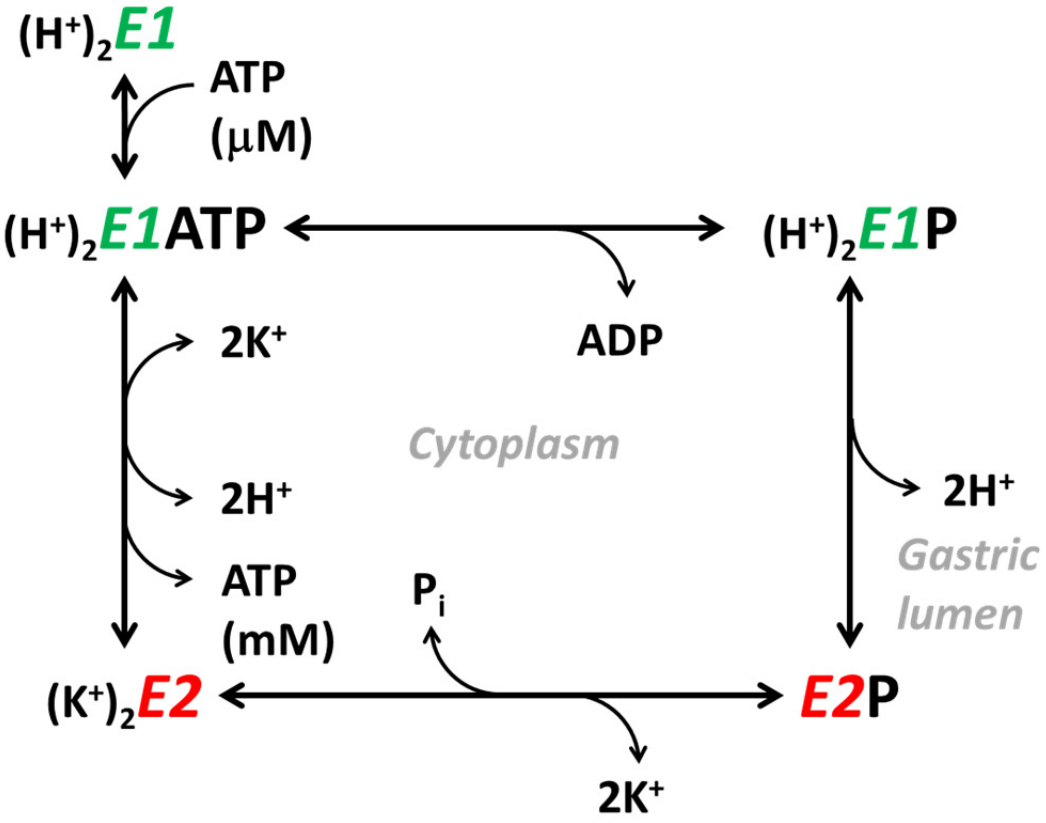

Fig. 1.3. 'Post-Albers'-type transport scheme of H^+,K^+-ATPase

Model of the ion transport cycle of the gastric H^+,K^+-ATPase is shown as a representative of P-type ATPases. Ion transport and ATP hydrolysis are coupled to the cyclic conversion of the enzyme (abbreviated as "E") between two reaction states, *E1* and *E2*, and their auto-phosphorylated form, *E1*P and *E2*P. In the *E1* state, H^+,K^+-ATPase has high affinities for cytoplasmic H^+ and ATP and a low affinity for luminal K^+. In the *E2* state, the H^+,K^+-ATPase has high affinity for K^+ but low affinity for H^+. Binding of ATP and subsequent transfer of the γ-phosphate to Asp residue of the invariant DKTG motif in the presence of Mg^{2+} generates the phosphoenzyme intermediates (*E1*P, *E2*P). Although Mg^{2+} is required for the auto-phosphorylation, it is not shown in this scheme for simplicity.

1.1.2. Transport cycle of P-type ATPases

Ion transport of all P-type ATPases is mediated based on a common principle, where the reversible phosphorylation of the conserved Aspartate plays a key role by facilitating the transition between two principal conformations with inwardly- and outwardly-facing binding sites for the respective transported cations. Conformational transition between these two states is linked to changes in the respective affinities for the transported cations, thus enable them to uptake of the ions from one side to the other (alternating access) [Widdas, 1952; Mitchell, 1957; Jardetzky, 1966]. The actual process is achieved through extensive conformational changes driven by ATP hydrolysis. Overall, the transportation cycle alternates between two conformational

states, the *E1* and *E2* states, as well as their corresponding phosphorylated form *E1*P and *E2*P states (Fig. 1.3, the scheme for H^+,K^+-ATPase is shown as a representative). The *E1* states are associated with auto-phosphorylation by ATP and have their ion binding sites opening to the cytoplasm with a high affinities for ATP (micromolar range) and the cation (*e.g.*, H^+ for H^+,K^+-ATPase, Na^+ for Na^+,K^+-ATPase and Ca^{2+} for SERCA) which is to be expelled from the cytoplasm. On the other hand, the *E2* states are associated with auto-dephosphorylation, and have their ion binding sites opening to the extracellular space. The *E2* states also have a low affinity to ATP (millimolar range) and the cations to be expelled from cytoplasm and a high affinity to the counterions (*e.g.*, K^+ for H^+,K^+-ATPase and Na^+,K^+-ATPase, and H^+ for SERCA). Phosphorylation by ATP of a conserved aspartate residue in the phosphorylation domain of ion-bound *E1* state forms the high-energy *E1*P state. This is followed by a subsequent conformational change to the functionally distinct lower-energy *E2*P state, which is associated with the opening of the ion binding sites towards the extracellular site. These conformational changes lower the affinity for the *E1*-bound cations. The *E1*-bound cations are then released and binding of counterions to the cation-binding sites induces re-occlusion and dephosphorylation of the transporter from *E2*P to *E2* state. Finally, the counterions are released during transition back to the *E1* state [Bublitz *et al.*, 2011]. This transport mechanism was originally proposed for the Na^+,K^+-ATPase (known as 'Post-Albers' scheme) [Albers, 1976; Post *et al.*, 1969] and was found to be conserved among the P-type ATPases, although different proteins transport different ions and with different stoichiometries.

1.1.3. Structure of P-type ATPase

The first high-resolution crystal structure of a P-type ATPase appeared in 2000 by [Toyoshima *et al.*, 2000], revealing the Ca^{2+}-bound *E1* state of SERCA at 2.6Å resolution (Fig. 1.4a). Compared to SERCA, structural elucidation of Na^+,K^+-ATPase [Morth *et al.*, 2007] lags far behind, and only cryo-EM structures of 6.5-8Å resolution have been reported for H^+,K^+-ATPase [Abe *et al.*, 2009; Abe *et al.*, 2010; Abe *et al.*, 2011; Abe *et al.*, 2012]. Along with the catalytic α subunit, these two P2C-type ATPases possess an accessary β-subunit (and γ-subunit only for Na^+,K^+-ATPase) which is necessary for function, thus substantially more complex than SERCA. These structures provide a basic architecture which is expected to be conserved for the catalytic subunits of all P-type ATPases (Fig. 1.4.b), that is, three cytoplasmic domains responsible for the ATP hydrolyzing activity, and transmembrane α-helices for ion transport. In the cytoplasmic domains, the nucleotide binding (N) domain functions to recognize ATP and position the γ-phosphoryl of ATP for nucleophilic attack, the phosphorylation (P) domain, which has the highest degree of conservation among P-type ATPases, contains a conserved aspartate residue which accepts the phosphoryl group and forms a high energy aspartyl-phosphate intermediate, and the actuator (A) domain positions water molecule for the subsequent hydrolysis which leads to the release of the phosphoryl group from the P domain [Bublitz *et al.*, 2010].

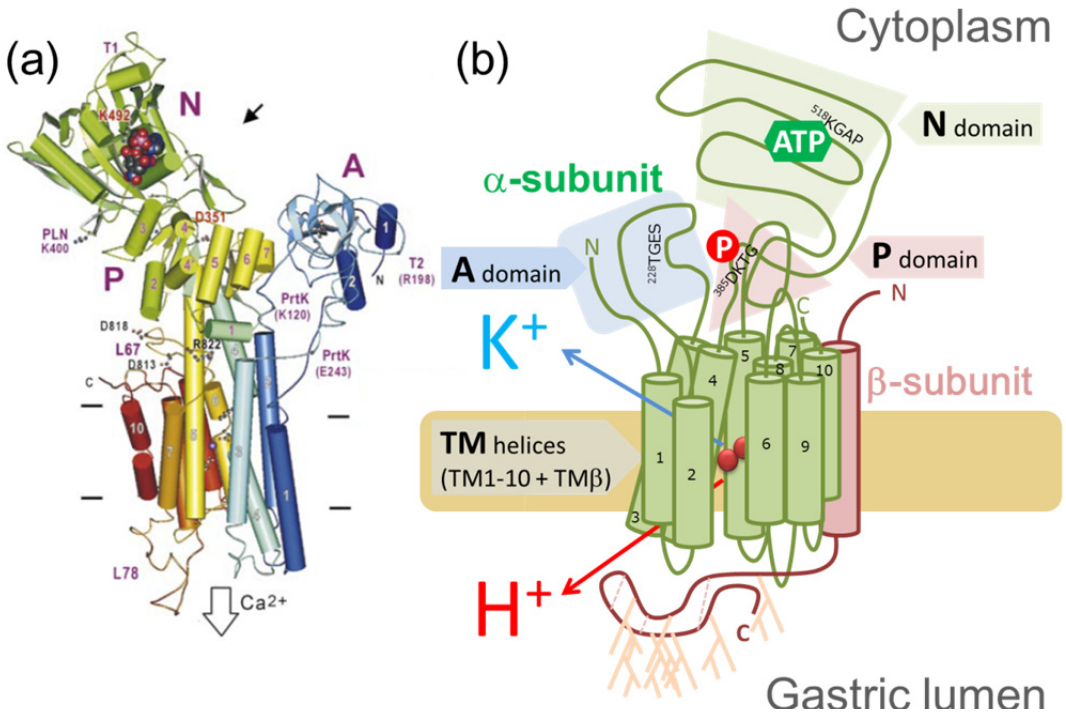

Fig. 1.4. Architecture of P-type ATPase

(a) The first high resolution structure of SERCA in the (Ca^{2+})*E1* state. Figure is from [Toyoshima *et al.*, 2000] with some modification. (b) A topology model of H^+,K^+-ATPase as a representative of P-type ATPase. Green columns indicate ten transmembrane (TM) helices of the α-subunit in which cation binding sites are located, and red column for TM helix of the β-subunit. Three cytoplasmic domains (A domain, blue; P domain, red; N domain, green) are shown with several conserved motif as indicated. Three disulfide bridges (dotted lines) and seven glycans (for pig enzyme, indicated as branched lines in white-pink color) are indicated in the ecto domain of the β-subunit.

1.1.4. Structure of SERCA

Following the first 3D structure of SERCA, additional structures in several different conformational states were reported, and now there are more than 30 entries of SERCA structures in PDB (protein data bank, www.pdb.org). Thus until now, SERCA is both structurally and functionally the best characterized member of the P-type ATPase, and its crystal structures in all major states of the reaction cycle are available (Fig. 1.5). From *E2* to *E1* state, the Ca^{2+} ions are binding to *E2*, straightens the M5 helix and breaks the closed configuration of the three cytoplasmic domains, exposing the catalytic site (note, this issue is discussed in chapter 4). Two Ca^{2+} ions are bound in the high affinity sites formed by transmembrane helices M4, M5, M6 and M8. The cytoplasmic gate is open and bound Ca^{2+} exchange with those in the cytoplasm. The M1 helix is deeply embedded in the lipid bilayer, stabilized indirectly by the bound Ca^{2+}.

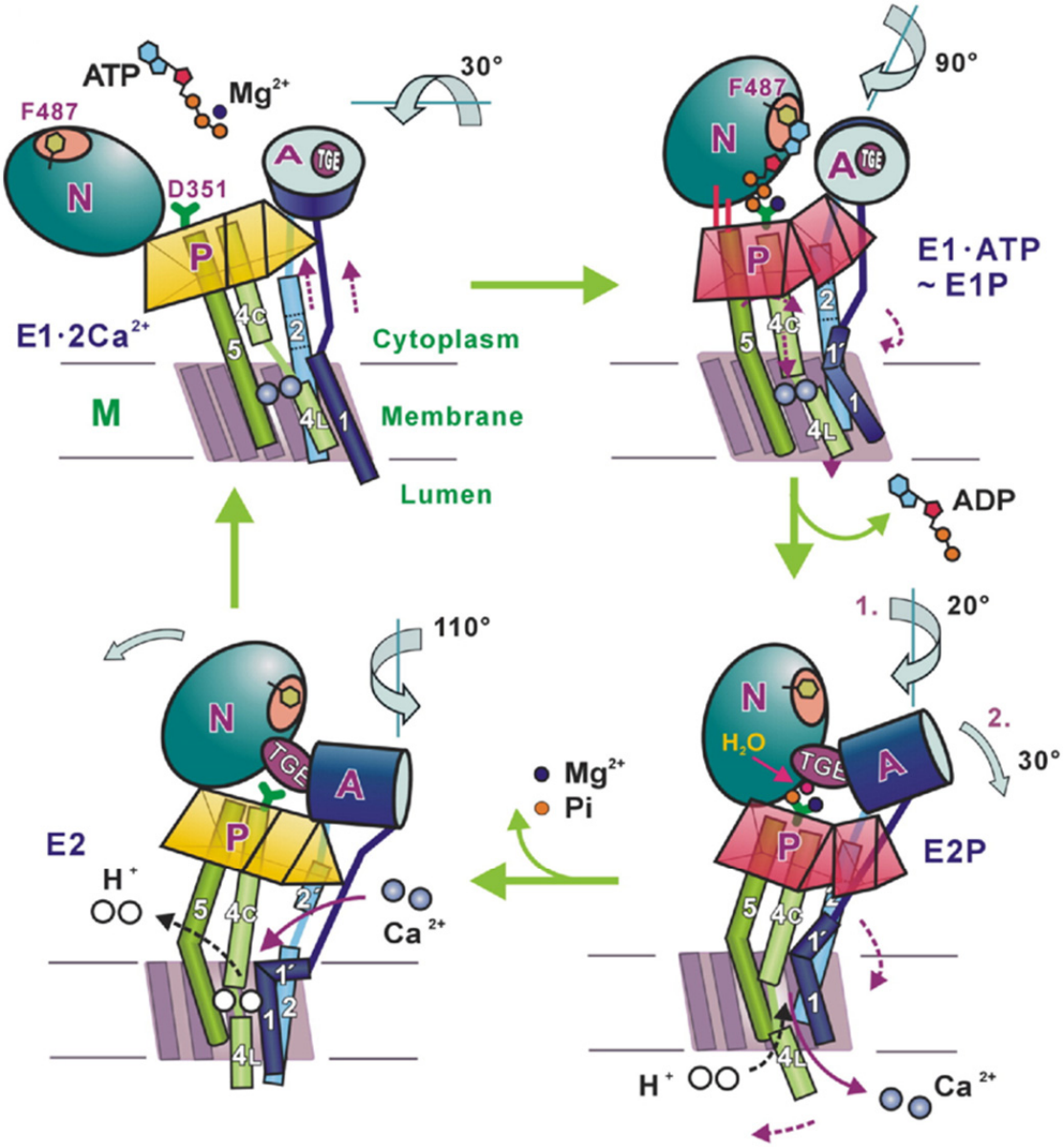

Fig. 1.5. Transport cycle by SERCA based on its structure

A cartoon depicting structure changes between different conformational states in the transportation cycle of Ca^{2+}-ATPase. In the *E1* state, the N domain is far from the P and A domain, making the aspartate 351 residue accessible to the outside ATP molecules. In the *E1*P state, ATP binds and crosslinks the P and N domains, making them close to each other. In the *E2*P state after the dissociation of ADP, the A domain rotates so that the TGES loop wedges into the gap and interacts with the phosphorylation site, resulting in the separation of N and P domains. These conformational changes in the cytoplasmic domains are connected with changes in the ion binding transmembrane domains, switching their ion affinities, and resulting in the translocation of ions. Figure is from [Toyoshima, 2009].

From *E1* to *E1*P state, ATP binds and crosslinks the P and N domains, so that the γ-phosphate of ATP and a Mg^{2+} bind to the P-domain to bend it. The N-domain is fixed in a highly inclined position and makes contact with the A-domain in a strained position. The M1 helix is pulled up and bent so that the top of the transmembrane part closes the cytoplasmic gate of the Ca^{2+} binding sites.

From *E1*P to *E2*P state, phosphoryl transfer to Asp 351 allows the dissociation of ADP, which triggers the opening of the N and P domain interface; the A domain rotates so that the TGES loop wedges into the gap and interacts with the phosphorylation site. This causes a marked rearrangement of the transmembrane helices M1–M6; large downward movements of M4, sharp bending of M5 and rotation of M6 destroy the Ca^{2+} binding sites. The lower sections of M1 and M2 push against M4L, opening the luminal gate and releasing the bound Ca^{2+} into the lumen.

From *E2*P to *E2* state, the TGES loop of the A domain fixes a particular water molecule and catalyzes its attack on the aspartylphosphate. The release of the phosphate and Mg^{2+} unbends the P domain. This in turn releases M1 and M2 so that M4L closes the luminal gate. The top amphipathic part of M1 forms a part of a cytoplasmic access funnel leading to Glu 309, the gating residue of the Ca^{2+} binding sites [Toyoshima, 2004].

1.2. Gastric proton pump, H^+,K^+-ATPase

1.2.1. The H^+,K^+-ATPase and its physiological role

The gastric H^+,K^+-ATPase is a membrane protein located in the parietal cell of the stomach. It stays in the cytoplasmic tubular membranes in the resting state and then moved to the microvilli of the expanded secretory canaliculus in the stimulated state of the parietal cell [Ganser and Forte, 1973; Forte *et al.*, 1983; Sawaguchi *et al.*, 2005]. It is responsible for secreting protons into the gastric lumen, generating a million-fold protein gradient across the gastric membrane and thereby acidifying the content of the stomach to a low pH up to 1 [Hersey and Sachs, 1995; Klaassen and De Pont, 1994; Rabon and Reuben, 1990; Wolosin, 1985].

The acidic environment of gastric lumen maintained by the gastric H^+,K^+-ATPase is important for food digestion and prevention of microorganism infection. It also makes the gastric H^+,K^+-ATPase one of the most sustainable target of therapeutic application in the regulation of acid suppression. In fact, recent development in therapy of acid disease such as peptic ulcer or gastroesophageal reflux disease has relieved heavily on the performance of drugs which inhibit the activity of gastric H^+,K^+-ATPase [Sachs *et al.*, 2007].

The gastric H^+,K^+-ATPase inhibitors discovered by now can be divided into two groups including the proton pump inhibitor (PPI) and potassium-competitive acid blockers (P-CABs). The PPIs such as omeprazole inhibit enzyme activity by covalently binding to the one or more cysteines (C813) of the gastric H^+,K^+-ATPase that are accessible to this large thiophilic cation from the luminal surface to alleviate the painful symptoms. Although PPIs have been very successful and effective, they

have disadvantages including dependence on an acidic environment, high acidity at night and short half-life [Sachs *et al.*, 2007]. The P-CABs such as SCH28080 and its derivatives inhibit H^+,K^+-ATPase noncovalently in a K^+-competitive manner from the luminal side of the enzyme. Compared with PPIs, the P-CABs are independent of an acidic environment and can suppress acid secretion rapidly [Shin *et al.*, 2009].

Besides its significant interest as a drug target, gastric H^+,K^+-ATPase faces a remarkable task of pumping protons against a million-fold gradient ranging from approximately pH 7 in the parietal cell to pH 1 in the stomach. Generation and maintaining a potent concentration gradient of six orders of magnitude is hardly achieved by any other P-type ATPases in nature. Therefore, understanding its molecular mechanism enable us to elucidate how the energetic challenges that membrane pumps are confronted with are met in living system.

1.2.2. The structure and transport cycle of H^+,K^+-ATPase

The gastric H^+,K^+-ATPase belongs to subfamily P2C in the P-type ATPases (Fig. 1.2). Its catalytic α subunit shows significant homology to other members in the P2-type ATPases, ~63% to the Na^+,K^+-ATPase and 25% to SERCA (Fig.1.1) [Sweadner and Donnet, 2001]. Like other P2C-type members, it is a heterodimeric enzyme containing two subunits of α and β (Fig. 1.4b). The catalytic α subunit consists of 1,033 to 1,034 (for pig enzyme used in this study) amino acids in length among all animal species and is about 110 kDa in weight [Rabon and Reuben, 1990]. It contains ten transmembrane segments (TM1 – TM10) and three cytoplasmic domains (the N, P and A domains). The transmembrane segments TM4, TM5, TM6, and TM8 contain a cluster of intramembranal carboxylic amino acids which form cation binding sites, and the cytoplasmic domains are responsible for ATP binding and provide energy to drive the active ions transport across membrane. The β subunit, which consists of 291 amino acids and is about 35 kDa with seven N-linked glycosylation sites (according to the pig sequence), is required for proper maturation and targeting of the enzyme to the plasma membrane [Chow and Forte, 1995].

Like other members of the P-type ATPase superfamily, the active exchange of protons and K^+ ions by H^+,K^+-ATPase across the cell membrane is driven by ATP hydrolysis with cyclical conformational changes between two principle reaction states (*E1* and *E2*) and their corresponding phosphoenzyme intermediates (*E1*P and *E2*P) (Fig. 1.3) [Rabon *et al.*, 1991; Stewart *et al.*, 1981; Wallmark *et al.*, 1980]. In the case of H^+,K^+-ATPase, proton binding to *E1* activates auto-phosphorylation of the enzyme at Asp385 by high-affinity MgATP binding and resulting in *E1*P state, which is soon converted to *E2P* state in the proton-transporting step to the gastric luminal side. Binding of K^+ to the *E2*P state accelerate dephosphorylation and the transition to the occluded form (K^+)*E2*, which subsequently change back to *E1* state as K^+ ions are released to the cytoplasm. During one cycle, the hydrolysis of one ATP molecule energizes the electroneutral transport of two H^+ and two K^+ ions in opposite direction in the neutral pH, although this stoichiometry is believed to be changed to one H^+ and one K^+ exchange per one ATP in the acidic pH of below 3.0 due to energy

requirement [Abe *et al.*, 2012; Munson *et al.*, 2003; Rabon *et al.*, 1982].

1.2.3. Recent development on 3D structural analysis of H^+,K^+-ATPase

Research on the gastric H^+,K^+-ATPase has been centered on functional study for decades, because its structural information has been missing and emerged in just recent years. The first 3D structure at 6.5Å of an intact gastric H^+,K^+-ATPase at aluminum fluoride (AlF)-bound *E2P* state was presented by the previous paper [Abe *et al*., 2009] using electron crystallography of 2D crystals (Fig. 1.6a). In this study, the N-terminal tail of the β subunit was found in direct contact with the P domain of the α subunit. This interaction stabilizes the enzyme conformation and prevents the reverse reaction from *E2*P to *E1*P state. Thus, the β-subunit N-terminus functions as a "ratchet", to ensure the transport cycle of the H^+,K^+-ATPase can only proceed in the forward direction, therefore resist the massive proton pressure across the gastric membrane [Abe *et al.*, 2009].

Another key requirement for the generation of the steep proton gradient is the transport stoichiometry. Because of the limited free energy available for ATP hydrolysis, the stoichiometry of transport cation must vary from $2H^+/2K^+$ to $1H^+/1K^+$ per hydrolysis of one ATP molecule as the luminal pH decreases below 3.0 [Munson *et al.*, 2003; Rabon *et al.*, 1982]. The 8Å structure of H^+,K^+-ATPase in Rb^+-occluded *E2*P state revealed that one but not two strong density located in its transmembrane cation binding site (Fig. 1.6b) highly likely represents a single bound Rb^+ ion, which is clearly different from Rb^+-free or K^+-bound structures. Measurement of radioactive $^{86}Rb^+$ binding suggests that binding stoichiometry varies depending on pH, and approximately half the amount of Rb^+ is bound under acidic crystallized conditions compared with the neutral pH. These data represent structural evidence of $1H^+/1K^+/1$ATP transport mode of H^+,K^+-ATPase, which is prerequisite for the 10^6-fold proton gradient across the membrane [Abe *et al.*, 2012].

The 3D structure at 7 Å of H^+,K^+-ATPase with bound representative P-CAB SCH28080 was reported. This study has provided the first structural evidence for a binding site of an acid suppressant on H^+,K^+-ATPase (Fig. 1.6c). However, the drug binding to the enzyme was not accountable by a simple "lock and key" model. The binding induced the widely-opened luminal cavity in the transmembrane domain, which is in turn transmitted to the cytoplasmic domains via connecting linker between them. The observed conformational change suggest that the mechanism, which generates the luminal-open conformation, is surprisingly conserved among H^+,K^+-ATPase and SERCA, and most likely such tightly coupled motion between two highly separated part of the enzyme (that is, cytoplasmic domains and transmembrane helices) provides a framework for all of P-type ATPases [Abe *et al.*, 2011] .

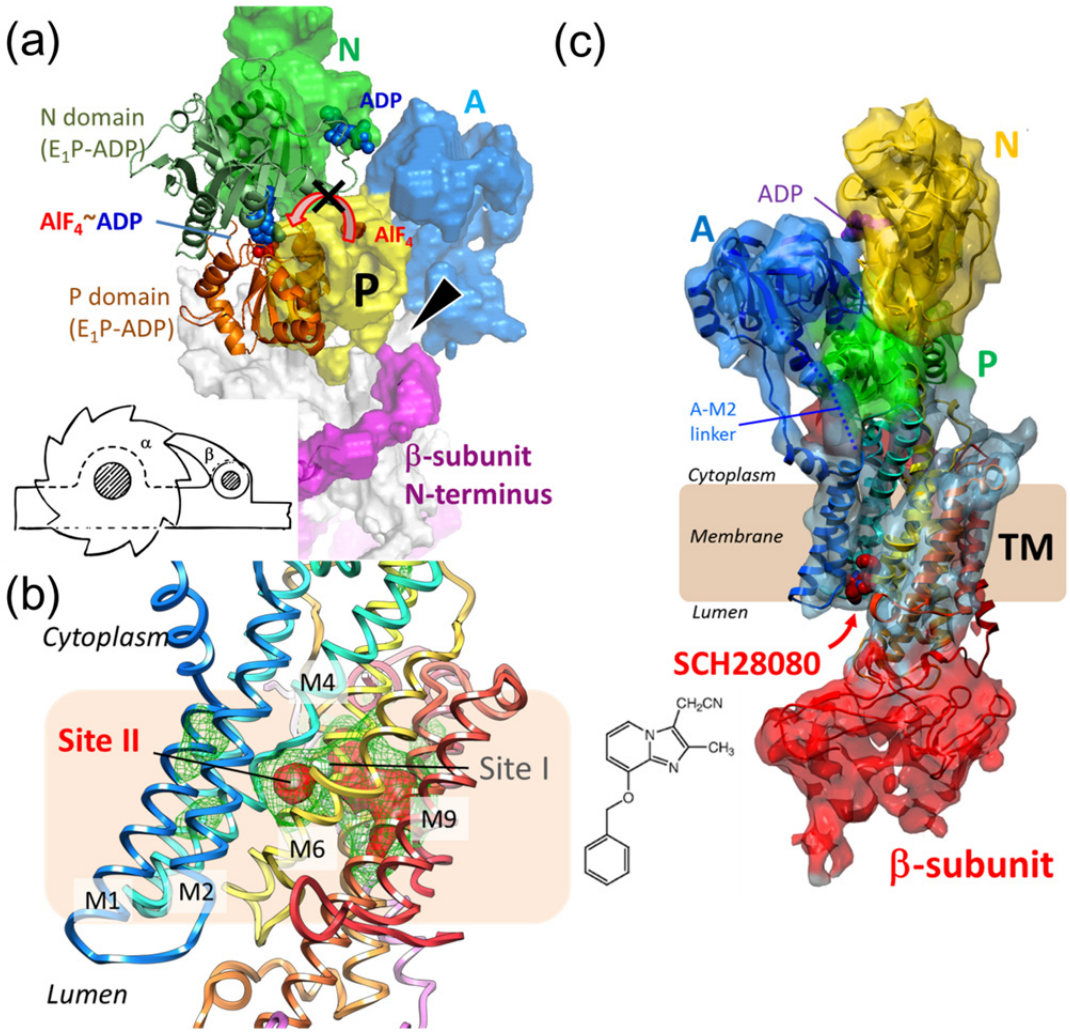

Fig. 1.6. Cryo-EM structures of H^+,K^+-ATPase

(a) A Ratchet model. The first 3D structure of H^+,K^+-ATPase reveals a unique inter-subunit interaction between P domain (yellow surface) and β-subunit N-terminus (magenta), which is act as a ratchet (cartoon in lower left) to prevent reverse reaction of the transport cycle (ref). (b) A single Rb^+-binding to the cation binding site. Red and green mesh represent a cryo-EM map of H^+,K^+-ATPase in (Rb^+)*E2*~P state contoured 5 and 4 σ, respectively, with superimposed homology model (ribbon). Figure shows enlarged view of the TM region. (c) A Cryo-EM structure of H^+,K^+-ATPase with bound a representative P-CAB, SCH28080 (chemical structure in lower left).

As described above, despite of their limited resolution, these structural and functional analyses provide important properties uniquely found for H^+,K^+-ATPase, *vice versa*, conserved mechanism among P-type ATPases. However, all of reported H^+,K^+-ATPase structures are limited to *E2*P-related conformations so far. For better understanding of the transport mechanism by H^+,K^+-ATPase, determination of structures of other principle conformational states (*e.g.*, *E1* , *E1*P and *E2* states) are highly desirable.

1.3. Electron crystallography

1.3.1. Electron crystallography as a method for structure determination of membrane proteins

Since the first 3D structure of membrane protein bacteriorhodopsin (bR) in 1975 [Henderson and Unwin, 1975], electron crystallography of 2D crystals has been a powerful technique, along with X-ray crystallography and nuclear magnetic resonance (NMR) spectroscopy, to study the 3D structure of biological macromolecules because of following reasons.

1. Because electron crystallography relies on 2D crystals in which membrane proteins are reconstituted in the lipid bilayer to form single- or double-layered two-dimensionally ordered array, structures can be analyzed in membranes that provide an environment similar to the native conditions [Fujiyoshi, 2011; Walz and Grigorieff, 1998].
2. Like X-ray crystallography, electron diffractions at high resolution obtained directly from the sufficiently large and well-ordered 2D crystals allow the building of an atomic model (*e.g.*, bR [Kimura *et al.*, 1997], the light-harvesting complex II [Kühlbrandt *et al.*, 1994], the acetylcholine receptor [Miyazawa *et al.*, 2003], aquaporins [Murata *et al.*, 2000; Hiroaki *et al.*, 2006; Tani *et al.*, 2009; Gonen *et al.*, 2004]).
3. Phases for the structure analysis are calculated directly from images. This characteristic provides a better quality map than dose X-ray crystallography at the same resolution [Fujiyoshi, 2011; Tani *et al.*, 2009; Ho *et al.*, 2009]. Moreover, 3D structure can be analyzed from their crystal images even when only poor-quality crystals are available, although resolution is strongly related to the crystal quality (*e.g.*, gap junction channels [Oshima *et al.*, 2007], H^+,K^+-ATPase [Abe *et al.*, 2009], bacterial sodium channels [Tsai *et al.*, 2013], *Euglena* tetraspanin IP39 [Suzuki *et al.*, 2013]).
4. In the 2D crystal, usually both sides of the specimen are kept open. Therefore effect of artificial crystal packing on the structure is minimized. Furthermore, this feature enables us to apply the freeze-trapping technique, which was used to elucidate the gating mechanism of acetylcholine receptor [Unwin and Fujiyoshi, 2012].

1.3.2. A practical procedure of electron crystallography using images

As described, an advantage of electron crystallography is that the 3D structure can be obtained even from small or moderately disordered 2D crystals. While these structures make valuable contributions to their respective field, it is also true that generating micron sized, well-ordered 2D crystals of membrane proteins is as challenging as generating 3D crystals used for X-ray. The 2D crystallization involves a lot of parameters which need to be optimized to produce good quality crystals.

These include a sufficient amount of target protein which should be purified to the highest possible degree of homogeneity, the detergent type and concentration in which the protein is stable, a suitable lipid to protein ratio (LPR), the buffer and device for dialysis, and other experimental factors.

The crystallization trails are screened and evaluated for their crystal size and quality by electron microscope. Usually, negative stain grids are prepared immediately following the dialysis since residual detergent might be left which could destroy the crystals or aggregation can occur with time. The grids are then scanned and qualities of the crystals are evaluated with their magnified images and their Fast Fourier Transform (FFT).

After extensive screening, crystals which appear to be good enough are further assessed by cryo-electron microscopy (cryo-EM). For data collection, 2D crystals are embedded in a layer of an amorphous ice, and the thinner ice layer is preferable. [Dubochet *et al.*, 1982; Fujiyoshi, 1998; Walz and Grigorieff, 1998]. However, thinner ice layer increases possibility of dehydration at which protein crystals are easily disordered. The single carbon preparation is the most commonly used method in which the solution embedding the crystals is placed on a single carbon film followed by rapid freezing. In this step, however, specimen is frequently too dehydrated to preserve inherent qualities of embedded crystals. Trehalose is commonly used as an embedding medium for 2D crystals owing to its high ability to preserve crystals in a vitrified specimen [Chiu *et al.*, 2011; Fujiyoshi, 1998; Hirai *et al.*, 1999]. However, 2D crystals of membrane proteins with large hydrophilic portion are much susceptible to specimen dehydration, and even trehalose embedding is insufficient to preserve their crystal qualities. Although the carbon sandwich technique was developed to improve specimen flatness, and beam-induced image shift in the tilted specimen (described later), we found that 2D crystals sandwiched between two sheets of carbon films was well preserved in their qualities (chapter 3).

Biological specimens are susceptible to radiation damage, and therefore, low-dose imaging techniques are used to limit specimen radiation as much as possible. A cryo-electron microscope equipped with a helium-cooled specimen stage by Fujiyoshi *et al.* has been achieved to reduce the effect of radiation damage by cooling specimen to 4 K [Fujiyoshi *et al.*, 1991].

A set of images is then obtained by tilting crystals to a variety of angles with the electron microscope. There is an innate limit in the tilt angle as crystal thickness increases dramatically above 60^{o} and becomes essentially infinite at 90^{o}, resulting in a missing cone of high-tilt data in the final dataset. Its effect on the final 3D map is however negligible because completeness in the reciprocal space is more than 87% and 94% if data can be collected up to 60º or 70º, respectively.

In the case of tilted specimen, however, beam-induced specimen charging cause a shift of the image vertical to the tilt axis, which results in a blurring of the image and thus a loss of information perpendicular to the tilt axis [Henderson, 1992]. Data from highly tilted images are, however, essential to build a 3D map, therefore strongly influence the quality of the resulting density map. In fact, because of this charging problem, data collection from 2D crystals of H^{+},K^{+}-ATPase in the *E1* state have been

limited only for the non-tilted specimen, although carbon sandwich preparation solve this critical problem as described later in chapter 3 and 4.

Recorded images are then digitized using a film scanner, and processed by MRC image processing programs developed by Unwin and Henderson [Henderson and Unwin, 1975; Crowther *et al.*, 1996], and further modified in our laboratory. This program package includes Fourier filtering to eliminate noise in each micrograph, unbending of the crystalline lattice based on the cross-correlation, and correction of contrast transfer function (CTF), to extract amplitude and phase information from each micrograph. These structural factors from non-tilted and tilted specimens are then merged into a set of lattice lines, and the final 3D density map is calculated [Fujiyoshi, 1998; Walz and Grigorieff, 1998].

1.4. Overview of this study

Since the first 3D structure of H^+,K^+-ATPase at *E2*P state in 2009, the structure information of H^+,K^+-ATPase at several *E2*P-related states have also been clarified. However, although research and attempts on the crystallization of H^+,K^+-ATPase in the *E1* state and its structural analysis have been carried out at the meantime [Nishizawa *et al.*, 2008], its 3D structure is still elusive due to poor crystal qualities as well as its susceptibility against dehydration occurred during ice embedding process for cryo-EM. In this study, for better understanding of the active transport mechanism by H^+,K^+-ATPase, which is able to generate more than a million-fold proton gradient across the membrane, we have attempted to analyzed its structure in the *E1* state by electron crystallography of 2D crystals.

In chapter 3, we showed the preservation effect on 2D crystals of carbon sandwich preparation for data collection by cryo-EM. In the sample preparation for cryo-EM, the ice thickness and preservation of the embedding crystals are crucially important. However, using the ordinary single carbon preparation in which the crystal solutions are loaded on a single carbon film, most crystals were broken and poorly ordered due to rapid dehydration of the specimen. To solve the problem, the carbon sandwich preparation in which the crystal solutions are sandwiched between two carbon films, prevents rapid dehydration and preserves the crystal condition giving much better quality with improved resolution. This preservation effect was especially important for 2D crystals of membrane proteins with large hydrophilic regions, such as H^+,K^+-ATPase. In addition, image shift occurred in most of the tilted specimens and even non-tilted specimens of H^+,K^+-ATPase crystals leading to a deterioration in image qualities in single carbon preparation while the effect is much more relieved in carbon sandwich preparation. Based on these results, the carbon sandwich preparation is demonstrated to be a better technique for efficient and high quality data collection of membrane proteins, compared with the single carbon preparation.

In chapter 4, by applying the carbon sandwich preparation, we were able to take images of 2D crystals of H^+,K^+-ATPase in the *E1* state with improved resolution and at a higher efficiency, compared to the previous results obtained by using the single carbon preparation [Yang *et al.*, 2013]. And based on these results, we have obtained

the first 3D structure of H^+,K^+-ATPase in the *E1* state analyzed at 14 Å. Different from the widely opened N domain found in X-ray structure of SERCA in the *E1* state, the conformation of the cytoplasmic domains, especially P and N domains, showed compact configuration in the EM map of H^+,K^+-ATPase *E1* state. This structural evidence is also supported by FITC fluorescence study which suggests hydrophobic environment of ATP-binding site at the N domain of H^+,K^+-ATPase *E1* state, indicating a close proximity between the N and P domains. This close orientation between ATP-binding site and auto-phosphorylation site of H^+,K^+-ATPase *E1* state might be helpful for the high-affinity ATP binding and subsequent phosphate transfer to the P domain, providing an advantage on the efficient turnover of the vectorial cation transport achieved by H^+,K^+-ATPase, and probably P-type ATPase in general.

CHAPTER 2

Materials and Methods

2.1. Purification of membrane-bound H^+,K^+-ATPase from pig stomach

2.1.1. Isolation procedures of membrane fractions

Procedures for the purification of the H^+,K^+-ATPase-enriched membrane fractions are based on [Chang *et al.*, 1977] with some modifications. Stomachs were obtained from freshly slaughtered hogs. Scrapings of hog gastric mucosa, after flooding with saturated NaCl to remove mucus, and 200 ~ 300 g of surface cells were homogenized by conventional food processor at 4ºC for 30 sec x 4 times with 1 min interval, in 0.25 M sucrose and 0.5 mM EGTA/Tris (pH 7.5). After removing debris by centrifugation, supernatant was further separated by centrifugation for 45 min at 36,000 rpm in a Beckman Ti70 rotor to collect crude microsomal fractions. White to pink-colored upper pellet was suspended by gentle vortex in 0.25 M sucrose and 0.5 mM EGTA/Tris (pH 7.5), and was separated further on a step gradient consisting of a layer of 7.5% (w/w) Ficoll on top of a 37% (w/w) sucrose layer in a Beckman Ti70 rotor by centrifuging for 90 min at 45,000 rpm. The fraction at the top of the gradient G1 and the fraction at the lower gradient G2 fractions were collected (Fig. 2.1a). G1 fraction is used for further purification based on [Yen *et al.*, 1990] (Fig. 2.1b) and is described as following.

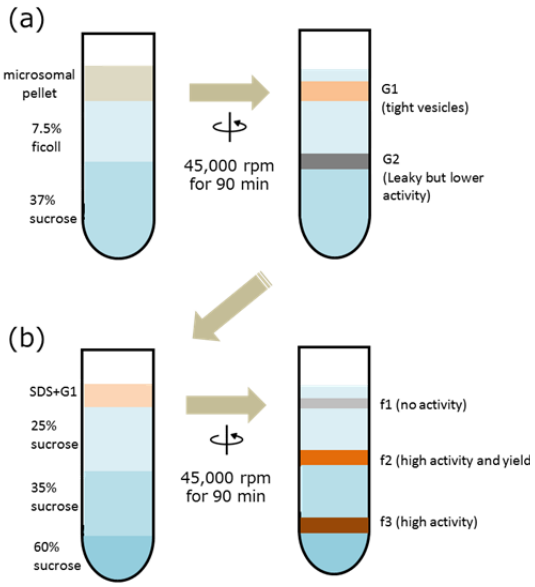

Fig. 2.1. Membrane fractions

(a) Separation of G1 G2 fraction from pig gastric microsomes. Crude microsomes were laid on a Ficoll density gradient, and separated in a G1 (light) and G2 (heavy) fractions. G1 fraction shows higher purity than G2 fraction. (b) After SDS-treatment, G1 fraction is further separated by sucrose stepwise centrifugation (f1, f2 and f3). The upper layer of f1 fraction has no activity. The middle layer of f2 fraction has high activity and high yield. The lower layer of f3 fraction has the highest activity with a much lower yield compared to f2. Fractions of f2 and f3 are collected for further experiments.

The G1 fraction (3 – 5 mg/ml) suspended in a buffer composed of 10 mM PIPES (pH 7.25 adjusted with Tris), 3 mM ATP/Tris (adjust pH 7), 0.5 mM EGTA/Tris and 20 % glycerol, is treated with 0 – 0.2% (w/v) SDS and incubated on ice for 10 min. Since G1 fraction contains ion-impermeable, inside-out tubular vesicles in which most of H^+,K^+-ATPase is embedded with their cytoplasmic-side out. Therefore, addition of small amount of SDS leaks tightly sealed vesicle, thus resulting increase in their specific activity (Fig. 2.2). The suitable SDS concentration to leak vesicle is variable in each lot of G1 fraction, which is related to the lipid composition of the

vesicles. Suitable SDS concentration for each lot of G1 was checked by titrating the G1 fraction in small scale before large scale purification as in Fig. 2.2 (usually SDS concentration used for the purification is between 0.12 to 0.16%).

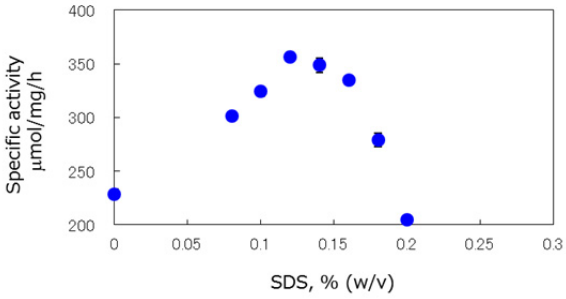

Fig. 2.2. SDS-treatment

ATPase activities of G1 fraction after titration with different concentrations of SDS. In the absence of SDS, the specific ATPase activity is relatively low because of the tightness of G1 vesicle. The specific ATPase activity is increased with increasing SDS concentration and gives a maximum at around 0.15% SDS in this lot of G1 fraction (1129 G1). On the other hand, too much SDS inactivates the enzyme.

The SDS-treated G1 fraction (2 mL) is then lay on a step gradient consisting of three layers of 25% (w/w), 35% (w/w) and 60% (w/w) sucrose in a Beckman Ti70 rotor by centrifuging for 90 min at 45,000 rpm (Fig. 2.1b). The G1 f2 and G1 f3 fractions were collected (Fig. 2.1b), diluted in 25 mM sucrose and 0.5 mM EGTA/Tris (pH 7.4), and spin down again in a Beckman Ti70 rotor by centrifuging for 90 min at 45,000 rpm. Finally, they were suspended in 250 mM sucrose, 0.5 mM EGTA/Tris, and 5 mM HEPES (pH 7.0). Purified membranes were frozen by liquid nitrogen, and stored at −80 °C until use.

2.1.2. Yield and purity

The amount of proteins, and specific activities in each membrane fraction was measured as in 2.2.1. and 2.2.2., respectively. The yield of ATPase activity in G1 f2 and G1 f3 from each lot of G1 fractions were listed in Table 2.1. The purity of each fraction is checked by SDS PAGE as shown in Fig. 2.3.

Table 2.1. Activity and yield of purified membrane fractions

Indicated parameters were determined in each purified membrane fractions. Activity recovery is calculated as total activity of each fraction per that of original G1 fraction.

lot #	sourse	p. conc. (mg/ml)	vol. (mL)	specific activity, (μmol/mg/h)	activity recovery (%)
0630 G1 f2	1129 G1	12.6	2.6	393	37.2
0630 G1 f3	1129 G1	7.5	0.6	416	5.1
0903 G1 f2	0226 G1	13.8	2.8	527	40.8
0903 G1 f3	0226 G1	10.6	1	673	14.3
0116 G1 f2	0225 G1	10.0	2.4	408	55.2
0116 G1 f3	0225 G1	7.6	0.8	472	16.0
1207 G1 f3	1023 G1	12	1.3	434	22.3
0908 G1 f2	0301 G1	18.5	2.4	573	53.0
0908 G1 f3	0301 G1	9.4	1	595	11.7

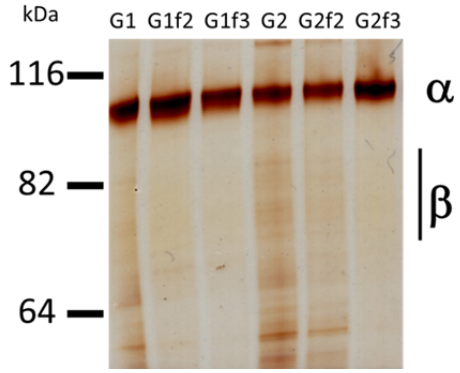

Fig. 2.3. SDS-PAGE analysis

SDS-PAGE analysis of purified membrane fractions detected by silver staining. In contrast to the α-subunit with apparent molecular weight of 110 kDa, the β-subunit gave smeared band distributed approximately 65-90 kDa due to heterogeneous glycosylation despite of its core molecular weight of 35 kDa.

2.2. Measurement of biochemical parameters

2.2.1. Protein concentration

The protein concentration was calculated by Bradford method, using bovine serum albumin as the standard [Noble and Bailey, 2009].

2.2.2. ATPase activity

Membrane-bound, detergent solubilized or 2D crystallized H^+,K^+-ATPase samples were diluted to a final protein concentration of about 5 µg/ml with reaction buffer (50 mM Imidazole, pH 7.0 (adjusted with HCl) 5 mM CH_3CO_2K, 1.5 mM $MgCl_2$ and 1.5 mM ATP/Tris and 250 mM sucrose for measurement of full ATPase activity in the membrane-bound enzyme, or 50 mM MES, pH 5.5 (adjusted with Tris), 100 mM CH_3CO_2K, 1.5 mM $MgCl_2$ and 1.5 mM ATP/Tris for the measurement of ATPase activities in the detergent-solubilized or crystallized samples. After 10 min at 37 °C the reaction was terminated by adding an equal volume of 12% SDS. The concentration of inorganic phosphate was determined colorimetrically by complexation with ammonium molybdate [Chifflet *et al.*, 1988].

2.2.3. Trypsin digestion

Prior to tryptic digestion, SDS-treated purified gastric membrane samples (0.5 mg/ml of protein) were incubated with the respective reaction buffers for 30 min at 25 °C. The reaction buffers contained 40 mM MES, pH 5.5 (adjusted with Tris) 1 mM $MgCl_2$ and 200 mM NaCl were added to the reaction buffer for the "Na^+" condition; 1 mM ADP, 4 mM NaF and 1 mM $AlCl_3$ (ADP were added before NaF and $AlCl_3$) for the "AlF-ADP" condition; 1 mM $BeSO_4$ and 4 mM NaF for the "BeF" condition; 10 µM SCH28080 for the "SCH28080" condition, and nothing for the "Free" condition. The reaction was initiated by adding trypsin to the samples. The trypsin concentration was adjusted (between 10 and 13 µg/ml) to obtain the same activity in the different buffers, using N_α-benzoyl-L-arginine-*p*-nitranilide (BAPNA) as a standard substrate. The reaction was terminated by adding 0.3 volume of Laemmli sample buffer

containing 3% SDS, 10 mM 2-mercaptoethanol, 100 mM Tris, pH 6.8 (adjusted with HCl) and 0.1% bromophenol blue. The time course of the trypsin digestion (10 s to 80 min) was analyzed by SDS–polyaclylamide gel electrophoresis (SDS–PAGE) using 8–16% polyacrylamide gradient gels (multi-gel II mini, Daiichikagaku). The gels were stained with Coomassie brilliant blue (CBB) based Simply Blue SafeStain (Invitrogen).

2.2.4. FITC fluorescence change

FITC modification of H^+,K^+-ATPase was performed as follows. Purified membrane fractions containing H^+,K^+-ATPase (G1 f2, 0.5 mg/ml) were incubated in 1 mM EDTA, 100 mM Tris/HCl (pH 9.2), 0.25 M sucrose and 10 μM of FITC dissolved in DMSO at 25 ºC for 30 min. The modification was terminated by the addition of 1 mM β-mercaptoethanol and the samples were washed twice with 10 mM HEPES/Tris (pH 7.0), 1 mM EDTA, 0.25 M sucrose. To estimate the amount of enzyme bound FITC, the FITC-modified H^+,K^+-ATPase preparations were incubated in a solution containing 1% (w/v) SDS, 100 mM Tris/HCl (pH 9.2) at room temperature for 1 hour and the absorbance at 495 nm (extinction coefficient 75,000 $M^{-1}cm^{-1}$ at 495 nm) was measured [Carilli *et al.*, 1982; Jackson *et al.*, 1983]. Amount of bound FITC to the H^+,K^+-ATPase preparation used in this study was 4.2 nmol/mg, which showed almost stoichiometric amount of bound FITC to the H^+,K^+-ATPase.

It is notable that the FITC-modification inhibited ATPase activity due to loss of the ATP-binding ability. However, as FITC modification and its inhibition can be competitively protected in the presence of high concentrations of ATP, the modification is specific to the ATP binding site at Lys518 of the α-subunit. Because FITC-modified H^+,K^+-ATPase can hydrolyze substrates less bulky than ATP such as acetyl phosphate or *p*-nitrophenyl phosphate (*p*NPP) [Abe *et al.*, 2005], FITC-modified enzyme is still active and undergoes conformational change in response to substrate binding, and therefore we could monitor conformational changes, especially occurred those in the N domain, by monitoring its fluorescence intensity [Rabon *et al.*, 1990].

FITC fluorescence change at the steady state was determined at 37 ºC in a 3 mL solution containing 50 mM HEPES/Tris, 1 mM $MgCl_2$, pH 7.0, 25 mM sucrose and 20 μg of FITC-labeled H^+,K^+-ATPase membrane fraction. Reactions were initiated by the addition of 300 μL of 5 M NaCl (final 200 mM) for "Na^+ (*E1*)", 75 uL of 2 M KCl (final 50 mM) for "K^+ (*E2*)", 10 μM SCH28080 for "SCH28080 (*E2*)", 5 mM $MgCl_2$ and 5 mM P_i for "Mg^{2+} + P_i (*E2*-P)", 1 mM $BeSO_4$ and 4 mM NaF for "BeF (*E2*-P)", or 5 mM $MgCl_2$ and 10 mM NaF for "MgF (*E2*·P)" conditions. Addition of same volume of 2 M Choline chloride is used as a control for "Na^+" or "K^+" conditions, because increase in ionic strength of the solution induce quenching of FITC fluorescence intensity. For other conditions, addition of reagents induced negligible effect on fluorescence intensity of FITC dye itself.

All measurement of FITC fluorescence were performed with a Shimadzu F5500 spectrophotometer, fitted with a magnetic device for stirring the cuvette's contents

and water temperature control. FITC fluorescence intensity was optimized by measurement at the wavelength pair ($Excitation_{495nm}$/$Emission_{515nm}$) with slit width set a 5 nm for either excitation or emission.

2.3. Two-dimensional crystallization of H^+,K^+-ATPase

2.3.1. The *E1* state

Two-dimensional crystals of H^+,K^+-ATPase at *E1* conformation were produced by a modified procedure from previous report [Nishizawa *et al.*, 2008]. The SDS-purified G1 fraction (G1 f2 or G1 f3, 2.5 mg/ml), which shows > 350 μmol P_i/mg/h specific ATPase activity, was solubilized for 10 min on ice with 1% (w/v) *n*-octyl-β-D-glucoside (OG) in 40 mM MES, pH 5.5, 20 mM $Mg(CH_3CO_2)_2$, 5 mM ATP, 10% (v/v) glycerol. After removal of the insoluble materials by centrifugation at 55,000 rpm for 20 min, the supernatant was mixed with *n*-oleoyl-D-sphingomyelin (Avanti) at lipid-to-protein ratio (w/w) of around 0.1, and the protein concentration and glycerol concentration in the supernatant were adjusted to 1 mg/ml and 35% (w/v) respectively. The samples were placed in 10 μl microdialysis buttons (Hampton Research) using a dialysis membrane with a molecular weight cut-off of 25 kDa (SPECTRA/Por #7, SPECTRUM). The samples were first dialyzed against 10 mM propionate, pH 3.9, 40% (v/v) glycerol, 1 mM $MgCl_2$ on ice for 12 h, then against 10 mM propionate, pH 3.9, 40% (v/v) glycerol, 5 mM $MgCl_2$ on ice for 2 days, and finally against 10 mM propionate, pH 3.9, 5 mM $MgCl_2$ on ice for 3 h. Crystal samples were removed from the dialysis buttons, and used within 6 h for negative stain for crystal screening, or sample preparations for cryo-EM observation.

2.3.2. The *E2*P and transition states during its dephosphorylation

Two-dimensional crystals of H^+,K^+-ATPase at *E2*P analogue conformation by using fluorinated phosphate analogs (Aluminum fluoride, AlF or Beryllium fluoride, BeF) were produced as described in [Abe *et al.*, 2009, 2010, 2012], and 2D crystals of H^+,K^+-ATPase at (SCH)*E2*BeF conformation, in which a representative K^+–competitive acid blocker SCH28080 is bound, were produced as described in [Abe *et al.*, 2011].

2.4. Specimen preparations for electron microscopy

2.4.1. Negatively-stained samples

Immediately after crystallization, 2 μl of the crystal solutions were put on the carbon coated metal plate and briefly mixed using peptide. After 1 min, the solution is removed with filter paper slowly and replaced by 3 μl of 2 % (w/v) uranyl acetate. The uranyl acetate was removed after several seconds followed by another 3 μl of the

same uranyl acetate. Finally, the uranyl acetate was removed completely and the negatively-stained samples were observed under electron microscope for screening of crystal frequency and quality.

2.4.2. Single carbon preparation

A small thin piece of carbon film was floated on dialysis buffer containing 7% (w/v) trehalose and picked up with a molybdenum grid. The solution containing H^+,K^+-ATPase 2D crystals (2 µl) was injected on the side of the grid opposite the carbon film and mixed well by pipetting. After removal of excess buffer, the grid was blotted for one or two times by filter paper with each blotting taking 1-5 seconds, and then dehydrated for 10-30 seconds depending on the environment, followed by plunge freezing into liquid nitrogen. The optimization of the vitrified ice thickness can be achieved by changing trehalose concentration, as well as time for blotting and dehydration. All steps were performed at 4°C.

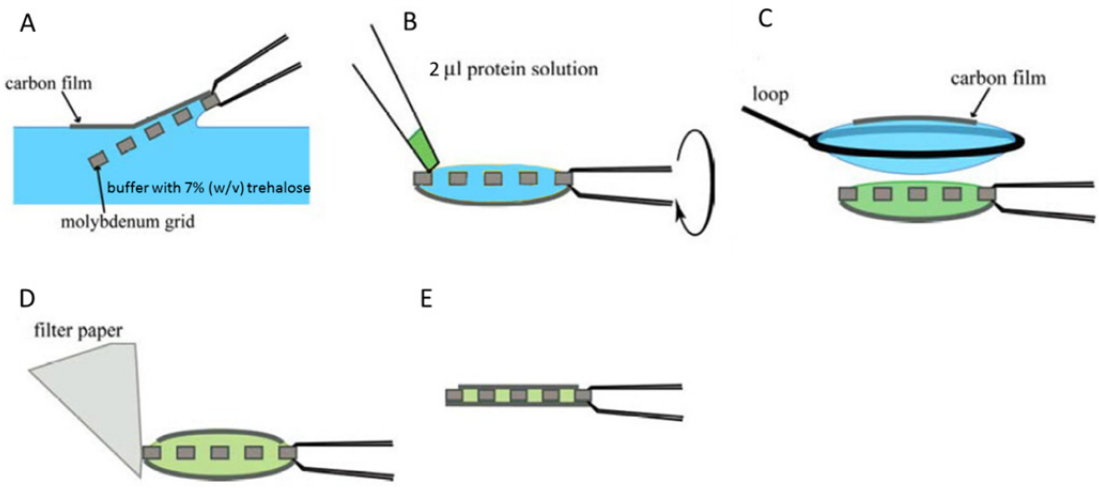

Fig. 2.4. Carbon sandwich technique

Specimen preparation by the carbon sandwich technique. (A) A piece of carbon film is floated onto buffer solution containing 7% (w/v) trehalose and picked up with a molybdenum grid. (B) The grid is turned over and 2 µl of protein solution is injected from the side opposite the carbon film and mixed. After several tens of seconds, excess liquid is removed. (C) A second piece of carbon film floated on buffer solution is picked up with a loop and deposited on the side of the grid that is not covered by the first carbon film. (D) Excess liquid is blotted away from the side of the grid with filter paper. (E) The final carbon-sandwiched specimen, which is ready for freezing.

2.4.3. Carbon sandwich preparation

Preparation by carbon sandwich preparation was performed as described by Gyobu et al. [2004], with some modifications (Fig. 2.4). A small thin piece of carbon film was floated on dialysis buffer containing 7% (w/v) trehalose and picked up with a

molybdenum grid. The side of grid without carbon film was wiped carefully by the middle part of pipette tip to remove excess carbon film from the grid edge. Two-microliter of H^+,K^+-ATPase 2D crystal solution was injected on the same side of the grid and mixed. After removal of excess crystal solution, a second piece of carbon film floated on the same dialysis buffer was picked up with a loop and deposited on the side of the grid without carbon film. Excess liquid was carefully blotted away by filter paper. The first few pieces of filter paper were put on the grid edge and remained for more than 20 s to ensure a continuous flow of liquid removal from the grid. The blotting step is especially important for optimization of the vitrified ice thickness, which usually takes 5 to 10 minutes in total when highly viscous samples such as glycerol-containing buffer are used. After removal of excess liquid, the grid was frozen by plunging into liquid nitrogen. All steps were performed at 4°C.

2.5. Electron microscopy and image analysis

Negative stained specimens were imaged using a JEM-1010 transmission electron microscope (JEOL) operated at 100 kV. For cryo-electron microscopy, images were recorded with a JEM-3000SFF electron microscope (JEOL) equipped with a field emission gun and a super-fluid helium stage [Fujiyoshi et al., 1991] and operated at 300 kV. Images were recorded on SO-163 film (Kodak) at a nominal magnification of 40,000x with a 2 s exposure and a total electron dose of 25 electrons/$Å^2$. The micrographs were developed for 14 min at 20^{o}C using full-strength Kodak D19 developer. The quality of the images was assessed by optical diffraction, and selected images were digitized with a SCAI scanner (Zeiss) using a step size of 7 μm. The digitized images were processed with the MRC image processing programs [Crowther *et al.*, 1996]. The crystal lattices were computationally unbent and corrected for the contrast transfer function (CTF) [Henderson *et al.*, 1986]. The initial CTF parameters for each image were determined by square frequency filtering combined with periodogram averaging [Tani *et al.*, 1996].

2.6. Structural analysis

2.6.1. Construction of electron-microscopic (EM) density map (EM map)

The data from 155 images were combined using LATLINE [Agard, 1983] and used to calculate a density map at 14 Å resolution. Extraction of the asymmetric unit (αβ-protomer of H^+,K^+-ATPase), and fitting of *E1* and *E2P* EM maps were carried out using UCSF Chimera [Pettersen *et al.*, 2004]. Figures are drawn using Chimera.

2.6.2. Homology model

The homology model for the H^+,K^+-ATPase *E1* structure was built with MODELER version 9.7 [Sali and Blundell, 1993] using the atomic model of the

E1P-ADP state of pig Na^+,K^+-ATPase (pdb code 3wgv) as a starting template. The initial manual fitting of the homology model into the EM density map was achieved using program O [Jones *et al.*, 1991]. The adjustment for each individual domain and TM helices with the EM map was performed using SITUS [Wriggers *et al.*, 1999]. After positional search, further fine fitting and connecting of the split loop regions were performed manually using O with regularization refinement.

CHAPTER 3

Carbon sandwich preparation preserves quality of two-dimensional crystals for cryo-electron microscopy

3.1. Summary

Electron crystallography is an important method for determining structure of membrane proteins. In this chapter, we show the impact of a carbon sandwich preparation on the preservation of crystalline sample quality using characteristic examples of two-dimensional (2D) crystals from gastric H^+,K^+-ATPase and their analyzed images. Compared with the ordinary single carbon support film preparation, the carbon sandwich preparation dramatically enhanced the resolution of images from flat sheet 2D crystals. As water evaporation is restricted in the carbon-sandwiched specimen, the improvement could be due to the strong protective effect of the retained water against drastic changes in the environment surrounding the specimen, such as dehydration and increased salt concentrations. This protective effect by the carbon sandwich technique helped to maintain the inherent and therefore best crystal conditions for analysis. Together with its strong compensation effect for the image shift due to beam-induced specimen charging, the carbon sandwich preparation is a powerful method for preserving crystals of membrane proteins with larger hydrophilic regions, such as H^+,K^+-ATPase, and therefore provides an efficient and high-quality method for collecting data for the structural analysis of these types of membrane proteins by electron crystallography.

3.2. Introduction

Since the first report of the three-dimensional (3D) structure of the membrane protein bacteriorhodopsin [Henderson and Unwin, 1975], electron crystallography of two-dimensional (2D) crystals has become a valuable approach for determining structure of membrane proteins [Fujiyoshi, 1998]. The ability to obtain structural information from 2D-ordered arrays makes this approach particularly useful for studies of membrane proteins in the lipid bilayer. Like X-ray crystallography, electron diffraction at high resolution obtained directly from sufficiently large and well-ordered 2D crystals allows for the construction of an atomic model [Glaeser *et al.*, 2007; Henderson *et al.*, 1990]. For phasing of the diffraction data, and especially for the structural determination of small or disordered 2D crystals, however, extraction of structural information from electron micrographs is a key requirement [Amos *et al.*, 1982; Fujiyoshi, 1998; Glaeser *et al.*, 2007; Henderson *et al.*, 1986; Henderson *et al.*, 1990].

In addition to the quality of 2D crystals themselves, several factors in sample preparation and data collection, such as lack of specimen flatness, radiation damage, dehydration, and image shift due to beam-induced specimen charging, can contribute to degrade image quality, and thus limit image resolution and efficient data collection [Fujiyoshi, 1998; Fujiyoshi, 2011; Henderson and McMullan, 2013]. Accordingly, numerous efforts have been made to improve and overcome these factors. To maintain 2D crystals in the hydrated state, methods for sugar embedding [Henderson and Unwin, 1975] and vitrified ice embedding [Dubochet *et al.*, 1982] have been introduced. Trehalose is a sugar best known in specimen preparation for its use as an embedding medium for 2D crystals [Chiu *et al.*, 2011; Fujiyoshi, 1998; Hirai *et al.*, 1999]. Due to its high ability to preserve crystals in a vitrified specimen, trehalose-embedding has been applied to many successful structural analyses of proteins such as bacteriorhodopsin [Kimura *et al.*, 1997] and aquaporins [Gonen *et al.*, 2005; Hiroaki *et al.*, 2006; Murata *et al.*, 2000]. In contrast to these examples, however, 2D crystals of membrane proteins with large hydrophilic portions are much more susceptible to specimen dehydration and also to changes in salt concentrations, and even trehalose-embedding is insufficient to preserve their crystal quality.

The carbon sandwich technique was developed by [Koning *et al.*, 2003] to improve specimen flatness, with some modifications introduced later by [Gyobu *et al.*, 2004]. In the carbon sandwich preparation, a solution containing 2D crystals is placed on a molybdenum grid that is sandwiched between two sheets of symmetric carbon films,

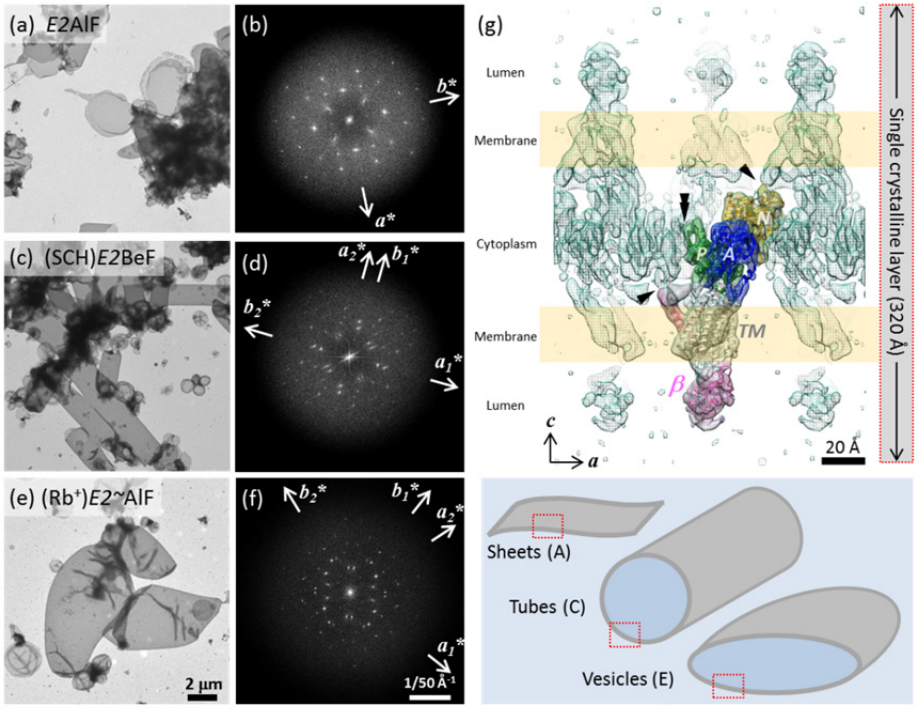

Fig. 3.1. 2D crystals of H^+,K^+-ATPase at different conformations

Negatively-stained 2D crystals of H^+,K^+-ATPase at different conformations show the variety in their morphologies. Flat-sheet crystals of *E2*AlF (a) consist of a single crystalline array, shown as a single reciprocal lattice in its Fourier transformation (b, indicated as *a** and *b**). On the other hand, flattened tubular crystals of (SCH)*E2*BeF (c) and vesicular crystals of (Rb^+)*E2*AlF (e), and their Fourier transformations (d and f, respectively) show two overlapping reciprocal lattices (*a1**, *b1** and *a2**, *b2**). Thus, each layer of these crystals was processed independently as two overlapping crystalline layers. Scale bars for crystal images and their Fourier transforms are shown in panel E (2 µm) and panel f (1/50 $Å^{-1}$), respectively. (g) Crystal packing of (SCH)*E2*BeF crystals shows that the inter-molecular contact between the N-terminal tail of β-subunit and the N domain (arrowhead), and the protruded structure of the P domain and the outermost portion of the A domain (double arrowhead) at the cytoplasmic side of the molecule. Color surface indicates EM map of H^+,K^+-ATPase αβ-protomer (blue, A domain; yellow, N domain; green, P domain; light gray, TM helices; pink, β-subunit) with a superimposed ribbon model. Green mesh indicates symmetry related neighboring molecules and wheat-colored boxes indicate approximate locations of lipid bilayers. Due to crystal packing, the single crystalline layer (indicated by a grey bar) consists of two lipid bilayers (indicated as wheat-colored boxes), which is responsible for the one crystalline layer of each crystal in the different morphologies (red dotted boxes in lower panel cartoon).

and excess liquid is blotted away from the side of the grid with filter paper prior to freezing. This preparation has been demonstrated to compensate for the image shift that is caused by beam-induced specimen charging, and therefore dramatically increases the yield of good images obtained at high-tilt angles [Gyobu *et al.*, 2004]. Besides its ability to compensate for the image shift, 2D crystals placed between two carbon films are expected to be better preserved in a hydrated state compared with standard single carbon support film preparations [Chiu *et al.*, 2011].

In this chapter, using 2D crystals of gastric H^+,K^+-ATPase, we demonstrate that the

carbon sandwich preparation better maintains the inherent crystal quality in cryo specimens than a single carbon preparation. Together with its strong compensation effect against image shift due to specimen charging, which is particularly critical when imaging tilted specimens [Gyobu *et al.*, 2004], the carbon sandwich preparation technique allows for the extraction of high-quality structural information from preserved 2D crystals, thereby enhancing data collection for 3D reconstruction.

3.3. Results and discussion

3.3.1. "Hydrophilic" 2D crystals from gastric H^+,K^+-ATPase

Gastric H^+,K^+-ATPase is an ATP-driven proton pump responsible for gastric acid secretion [Ganser and Forte, 1973], that comprises a catalytic α-subunit (~100kDa) and an accessary β-subunit (~35 kDa). The α-subunit contains 10 transmembrane helices in which cation-binding sites are located, and large cytoplasmic domains (A, P, N domains) where ATP-hydrolysis occurs; the large cytoplasmic domains comprise ~70% of the total mass of the α-subunit [Toyoshima *et al.*, 2000]. The β-subunit has a single transmembrane helix with a short (~30 amino acids) N-terminal cytoplasmic tail and a C-terminal ectodomain. Like other P-type ATPases, vectorial cation transport is accomplished by cyclical conformational changes between two principle functional states (*E1* and *E2*) and their corresponding phosphoenzyme intermediates (*E1P* and *E2P*) [Robon and Reuben, 1990].

Successful 2D crystallization of gastric H^+,K^+-ATPase has yielded 2D crystals with different morphologies, including sheets (Fig. 3.1a,b) [Abe *et al.*, 2009], tubes (Fig. 3.1c,d) [Abe *et al.*, 2010; Abe *et al.*, 2011; Nishizawa *et al.*, 2008], and vesicles (Fig. 3.1e,f) [Abe *et al.*, 2012], depending on the conformational state of the protein and other crystallization conditions, although their crystal packing is essentially the same (Fig. 3.1g). Single crystalline sheets consist of two membrane layers, and the proteins in the two membrane layers are related to the each other by a two-fold screw axis, resulting in a $p22_12_1$ symmetry. Thus, the crystal ideally forms planar crystalline arrays like the single-layered sheet crystals found in the *E2*AlF conformation (Fig. 3.1a,b). For tubular crystals (Fig. 3.1c,e), however, they are too thick to apply a helical symmetry like the thin tubular crystals of acetylcholine receptors [Miyazawa *et al.*, 2003]. Thus, as is the case for vesicular crystals, tubular crystals are analyzed as two overlapping layers of crystalline sheets (Fig. 3.1d,f). Due to its characteristic crystal packing, all of the inter-molecular contacts in the H^+,K^+-ATPase 2D crystals can be found at the

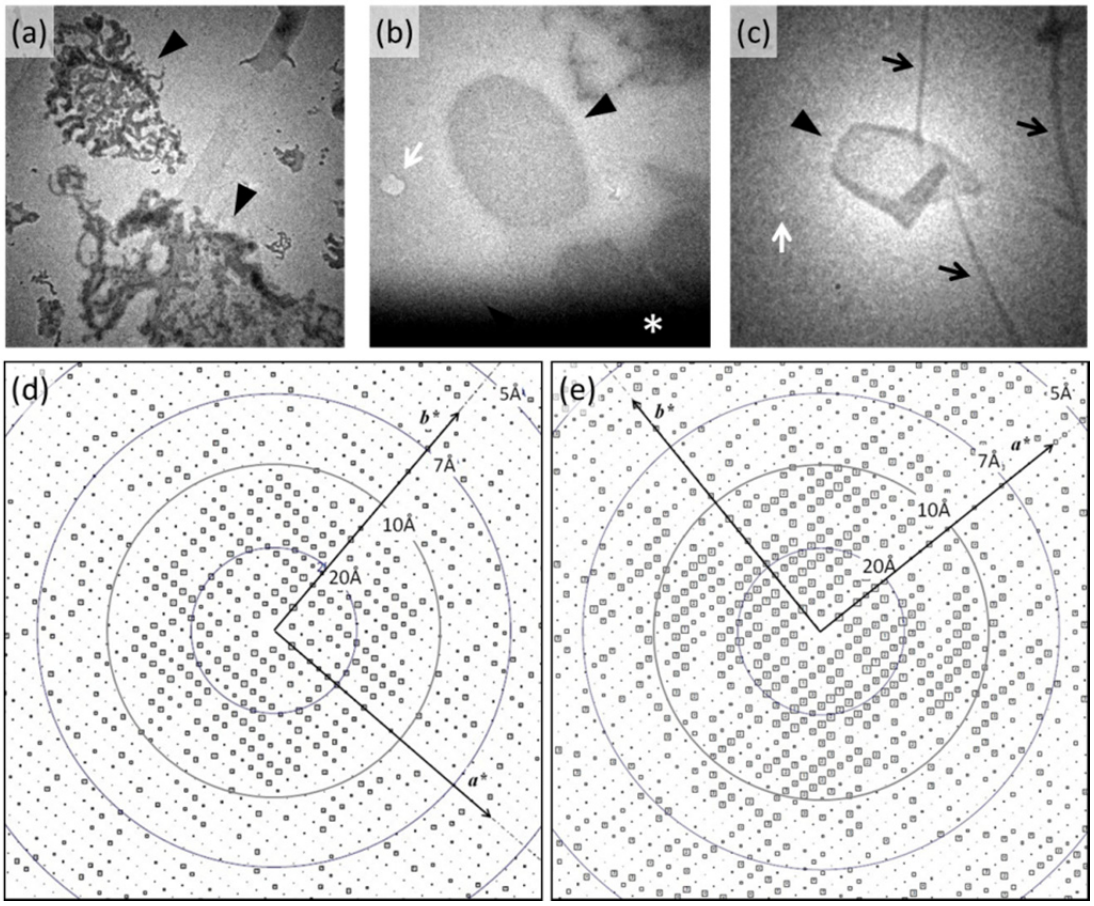

Fig. 3.2. Comparison of the analyzed image quality between carbon sandwich and single carbon support film preparations.

(a-c) Low magnification images (search mode) of H^+,K^+-ATPase 2D crystals (arrowheads) in frozen specimens prepared by the single carbon method (a,b) or carbon sandwich method (c). Most of the crystals embedded in the thin ice are dehydrated in the single carbon preparation (a), while preserved crystals can be found in the thicker ice area at the edge of the grid well (*: dark area) in some cases (b). In the carbon sandwich preparation, preserved 2D crystals are distributed evenly over the grid well (c). White arrows indicate the position used for focusing the image, and black arrows indicate crinkling of the carbon membrane, which usually occurs in carbon sandwich preparations. Because all images herein were obtained using a low-dose defocused diffraction mode, the mean diameter of ~2 µm for sheet crystals is used for approximate scaling. (d,e) IQ-plot calculated from a non-tilted image of H^+,K^+-ATPase single sheet crystal in the *E2*AlF conformation prepared by the single carbon support film (d) and carbon sandwich (e) techniques.

cytoplasmic portions of the molecules (Fig. 3.1g), in marked contrast to relatively hydrophobic membrane proteins such as bacteriorhodopsin or aquaporins. Therefore, 2D crystals of H^+,K^+-ATPase are expected to be more susceptible to dehydration than those hydrophobic proteins.

3.3.2. Carbon sandwich effectively preserves the crystal quality

Trehalose-embedding has been applied for the successful structural analysis of several membrane proteins by preserving 2D crystals in the hydrated state [Chiu *et al.*, 2011]. When we applied standard single carbon support film preparations for apparently flat sheet crystals made of decylmaltoside-solubilized H^+,K^+-ATPase in the presence of AlF adopting a *E2*AlF conformation (Fig. 3.1a), most of the crystals were obviously broken (Fig. 3.2a) and poorly ordered, as evaluated in the optical diffraction. Exceptions were observed at the edge of the grid well (indicated by the * in Fig. 3.2b), in which remaining embedding buffer provides relatively thicker vitrified ice than that in the center of the grid well (Fig. 3.3a). In such a wet environment, some of the crystals were preserved and diffraction spots reach ~10 Å resolution (Fig. 3.2d) in its calculated Fourier components (IQ-Plot) [Henderson *et al.*, 1986].

Using the same batch of 2D sheet crystals of *E2*AlF H^+,K^+-ATPase, the qualities of non-tilted images prepared by the carbon sandwich technique (Fig. 3.2c) were compared with those supported by a single carbon film. Non-tilted images from the carbon sandwich preparation can reach up to 7Å of resolution (Fig. 3.2e), while those from single carbon preparations are limited to a resolution of 10Å (Fig. 3.2d). The effect of the beam-induced image shift is excluded in this case because an isotropic Thon ring is clearly visible in the calculated Fourier transformation of both preparations under non-tilted conditions. Therefore, the remarkable difference in resolution is due to preservation of the 2D crystal quality during specimen preparation on the EM grid (Fig. 3.3). In carbon sandwich preparations, the crystals are sandwiched between two carbon films and are thus likely protected from rapid dehydration (Fig. 3.3b), while in single carbon preparations the upper surface is in direct contact with the air atmosphere, and water is easily evaporated causing excess dehydration as well as associated changes in the embedding buffer such as variable salt concentrations (Fig. 3.3a). The H^+,K^+-ATPase molecules are interconnected at their hydrophilic part to form crystals in the 2D crystallization process (Fig. 3.1g). Thus, excess dehydration and/or concentration changes of the reagents in the embedding buffer may destroy both the inter- and intra-molecular interactions, leading to deterioration of the inherent crystal quality and even the original protein structure itself. In fact, a change in pH and/or salt concentration in the embedding buffer caused by washing 2D crystals on the grid induced disorder of the crystals within several seconds, as determined by negatively-stained samples (data not shown). In the carbon sandwich preparations, the thickness of the water layer on the EM-grid becomes thinner for a longer time by

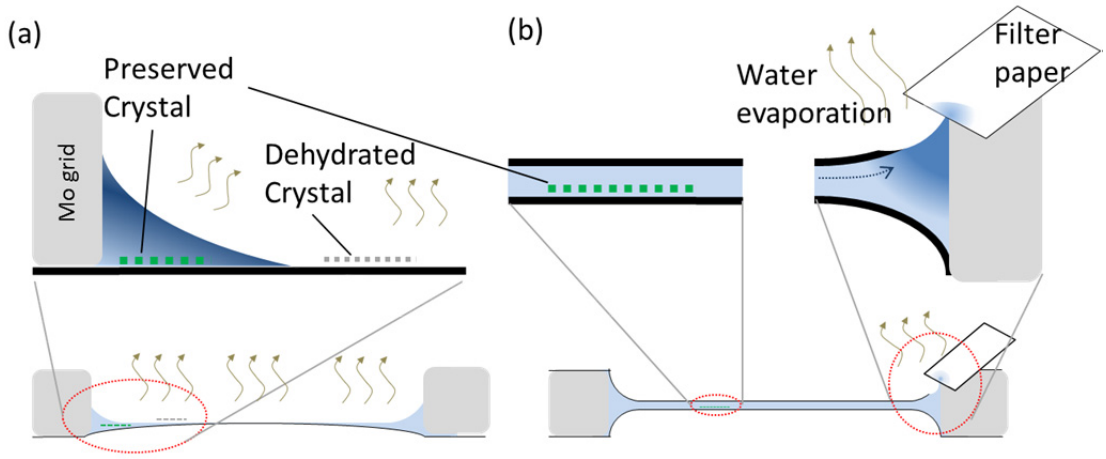

Fig. 3.3. Cartoons of single carbon and carbon sandwich preparations

Cartoons depicting the cross section of the specimen prepared by single carbon preparation (a) and that by carbon sandwich preparation (b). Black lines indicate carbon support films, grey boxes indicate the molybdenum grid, and light blue indicates the embedding buffer. As water evaporated (tan wavy arrows) from the surface of the specimen (a), most of the crystals were broken by dehydration (grey dotted line). Preserved crystals (green dotted line) were always observed in the thick ice at the edge of the grid (Fig. 3.2b), while the resolution is limited (Fig. 3.2d) due to the increased concentration of the embedding buffer by dehydration (dark blue). In contrast, water evaporation occurred only at the blotting position where the upper carbon membrane was partially broken by filter paper in the carbon-sandwiched specimen (b). Thus, the concentration change of the embedding buffer was limited around 2D crystals sandwiched between two carbon films (Fig. 3.2c), while the salt concentration was increased at the blotting position (b). Removal of excess water by blotting or evaporation induced spontaneous water flow (dotted arrow), which may prevent free diffusion of concentrated reagents to the central area of the grid. Therefore, the microenvironment of the 2D crystals embedded in the thin water layer seems to remain constant during preparation, and thus the inherent crystal qualities are preserved in the carbon sandwich preparations (Fig. 3.2e).

continuous blotting and spontaneous evaporation at the edge of the covered piece of carbon film (Fig. 3.3b). Because such events may induce spontaneous water flow toward the blotting position (indicated by the dotted arrow in Fig. 3.3b), free diffusion of the concentrated reagent from this position should be suppressed. Therefore, while the salt concentration is increased around the blotting position (indicated as the dark blue region at the edge of the specimen in Fig. 3.3b), the salt concentration of the solution in most of the other area, which contain many crystals (light blue region in Fig. 3.3b), is presumed to be less variable. Compared with the single carbon preparation, the carbon sandwich preparation protects the 2D crystals from environmental changes such as dehydration as well as salt concentration variability, and thus structural information can be extracted with its full potential for electron crystallography.

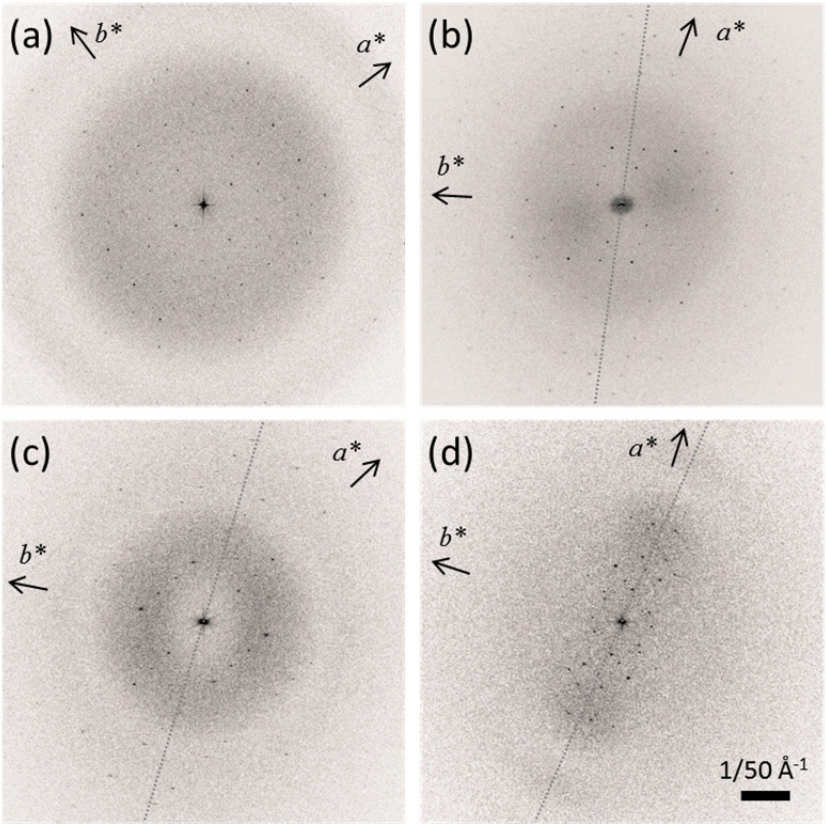

Fig. 3.4. Fourier transforms from carbon sandwich preparation

Representatives of Fourier transforms of a crystal image taken from non-tilted (a), 45° (b) and 70° (c) tilted specimens prepared by carbon sandwich preparation, show isotropic diffraction spots as well as Thon rings, and are thus well suited for image processing [Abe *et al.*, 2009]. In contrast, spots just along the tilt axis (dotted lines) are visible in the Fourier transform of 20° tilted crystals from single carbon preparation due to beam-induced specimen charging (d). Reciprocal lattice vectors (*a*, b**) are indicated as arrows, and tilted axes are shown as dotted lines in tilted data. A scale bar is shown in panel D (1/50 $Å^{-1}$)

3.3.3. Compensation effect of carbon sandwich preparation against beam-induced image shift

Image shift due to beam-induced specimen charging causes diffraction spots perpendicular to the tilted axis to disappear in the Fourier transforms of images, even at medium or low resolution, as shown in Fig. 3.4d. The efficiency of isotropic data collection without deterioration of images of the tilted specimen is therefore another key requirement for determination of the 3D structure with a reduced missing cone effect. In the case of H^+,K^+-ATPase 2D crystals, the image shift severely affects the crystal images obtained from single carbon preparations, presumably because this molecule forms thicker 2D crystals that accumulate more charge than thinner ones. It is notable that more than 20% of micrographs are affected by image shift, even those of non-tilted specimens, and no micrographs without an image shift have ever been obtained from tilted specimens prepared by a single carbon support film (Table 3.1). In contrast,

Table 3.1. Statistics of the data collection for structural analysis of H^+,K^+-ATPase in different conformations

Table shows numbers of 'micrographs' used for the structural determination of the indicated conformation of H^+,K^+-ATPase (see chapter 2 Materials and Methods for details). Number of micrographs obtained (blue rows), selected for scanning (green rows), processed by MRC program (yellow rows) and finally merged into a 3D structure (red rows) are indicated. Because all of the tilted images were affected by the image-shift due to specimen charging in the case of the single carbon preparation of the *E2*AlF crystals, micrographs with recognizable diffraction spots in the direction parallel to the tilt axis (as shown in Fig. 4d) were selected.

Conformation	Preparation	Cryo grids used	Micrographs						Resolution	Phase residual	Ref.
			Tilt angles					Total			
			0	20	45	60	70				
*E2*AlF	single carbon	121	-	-	-	-	-	-	-	-	-
			-	-	-	-	-	-			
			59	10[a]	28[a]	-	-	97			
			328	465	420	-	-	1213			
*E2*AlF	carbon sandwich	182	7	48	92	118	54	319	6.5 Å	31.5	Abe *et al.* 2009
			70	120	202	206	119	717			
			86	205	311	262	217	1081			
			274	584	660	430	349	2297			
*E2*BeF	carbon sandwich	47	11	20	57	-	-	88	8 Å	33.1	Abe *et al.* 2010
			38	24	73			135			
			47	64	90	-	-	201			
			120	156	286	-	-	562			
(SCH)*E2*BeF	carbon sandwich	97	6	43	128	118	-	295	7 Å	37.1	Abe *et al.* 2011
			14	53	203	210		480			
			15	59	278	249	-	601			
			70	90	542	403	-	1105			
(Rb^+)*E2*AlF	carbon sandwich	78	3	18	68	57	-	146	8 Å	35.6	Abe *et al.* 2012
			9	29	88	116		242			
			42	87	208	202	-	539			
			80	275	410	402	-	1167			
(K^+)*E2*AlF	carbon sandwich	125	6	34	54	69	-	163	8 Å	36.9	Abe *et al.* 2012
			38	73	118	126		355			
			80	100	180	204	-	564			
			443	588	430	551	-	2012			

although the success ratio for collecting images of bacteriorhodopsin 2D crystals was not very high, the quality of ~2% of the images was high, even those obtained at a 60°tilt. Because of the hydrophilic molecular packing in H^+,K^+-ATPase crystals, preserved crystals are always embedded in relatively thick vitrified ice, which can usually be found at the edge of the molybdenium grid well in single carbon preparations (Fig. 3.2b and Fig. 3.3a), such a thick specimen area more easily accumulates charges that deflect the electron beam and cause an image shift [Gyobu *et al.*, 2004]. More importantly, the ice thickness, which is steeply variable on the edge of the specimen as seen in Figs. 3.2b and Fig 3.3a, accumulates charge unevenly, resulting in more serious deflection of the beam. This is another reason why more than 20% of micrographs of H^+,K^+-ATPase crystals are affected by an image shift even in non-tilted specimen conditions, while all images of bacteriorhodopsin crystals in the non-tilted condition provided isotropic data in their Fourier transforms.

Consistent with a previous study on aquaporin-4 crystals [Gyobu *et al.*, 2004], the carbon sandwich preparation dramatically improved the efficiency of data collection

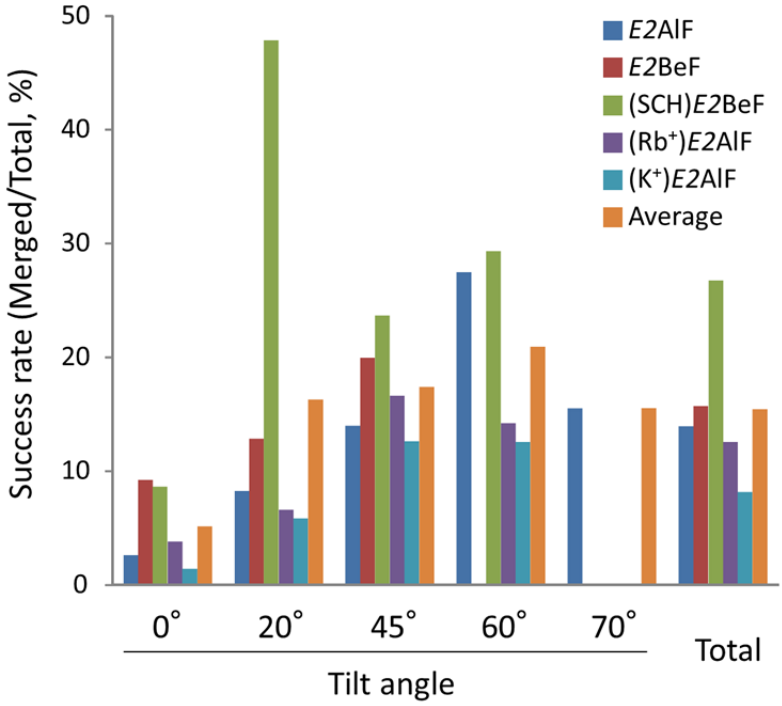

Fig. 3.5. Data collection from carbon-sandwiched specimens

Statistics of data collection from carbon-sandwiched specimens. Success rate was calculated from the number of micrographs merged into the 3D structure factor per total micrographs obtained, for each crystal sample in a different conformation of the transport cycle as indicated by different colors in the figure.

even from samples susceptible to beam-induced image shift (Fig. 3.4). While the success rate depended on the specimen thickness as well as the surrounding conditions of the specimen, including the objective-lens aperture, fewer than 10% of images were affected by beam-induced image shift for a 20° tilted specimen and fewer than 30% to 40% of images were affected by a beam-induced image shift for a greater than 45º tilted specimen (Fig. 3.4a-c). Isotropic data can be successfully collected even from 70º tilted carbon-sandwiched specimens (Fig. 3.4c), while, even at 20º tilted specimen, diffraction spots and a Thon ring perpendicular to the tilt axis disappeared in the Fourier transform of the crystal image produced by a single carbon preparation (Fig. 3.4d).

3.3.4. Efficiency of data collection achieved with carbon sandwich

Statistics of the data collection for the structural analysis of H^+,K^+-ATPase in different conformations as well as by two specimen preparation techniques in the E2AlF state are summarized in Table 3.1. Qualities of all of the micrographs obtained (blue rows) were assessed by optical diffraction, and selected images were digitized (green rows). In this step, except for single carbon prepared samples, micrographs with

poorly-ordered crystals and/or beam-induced image shift were excluded (58% of total micrographs). Selected micrographs (42% of total micrographs) were then processed using the MRC image processing program, and selected manually based on the amplitudes of IQ plots (yellow rows). The acceptable images (27% of total micrographs) were further selected by phase residual cut-off, and finally ~15% of the total micrographs obtained were merged into the 3D structure factor (red rows). These results markedly contrast with the statistics of the single carbon preparation, by which no structure could be analyzed regardless of how many images were obtained (1213 images).

Statistics of the success rate for merging (*i.e.*, number of micrographs merged/total) are summarized in Fig. 3.5. To obtain a reliable structure, analyzed data were carefully selected according to their phase residuals and amplitude IQ values, as indicated above. Because strict criteria for the selection were set, especially for 0° and 20° tilted data, the success rate in these lower tilt angles was limited, except for a 20° tilt of (SCH)*E2*BeF, compared with those having high-tilt angles. There was an exceptionally high success rate in the 20° tilted (SCH)*E2*BeF crystal (48% of total micrographs obtained taken were merged into the 3D structure factor), in marked contrast to the success rate of other 20° tilted data (6-16%). The reason for this is that all of the micrographs were obtained from only two successfully prepared grids. As seen in this example, and also the inconsistent success rates among other preparations, there was a large variety in the degree of preservation among carbon sandwich-prepared specimens. On the other hand, the (K^+)*E2*AlF crystal had the lowest success rate among all the crystal samples (8% in average of all tilted angles), which cannot be explained by the variation in specimen preparation alone. Thus, the low efficiency in the (K^+)*E2*AlF statistics is most likely due to the inherent quality of the crystals as well as their stability during specimen preparation. For H^+,K^+-ATPase samples, successfully or poorly preserved crystals are hardly distinguishable based on their morphology alone in the low-dose search mode, and data collection still relies on trial-and-error due to the large variation in crystal preservation. The average success rate of 15% is the mean of the values of 30% and 0%, rather than an even distribution of ~15% preserved crystals. This indicates that further improvement of the reproducibility of crystal preservation is needed for efficient data collection.

3.3.4. Concluding remarks

In this study, we show that the carbon sandwich preparation contributes to preserve

the inherent crystal quality. Preservation of the hydrated environment of 2D crystals made of membrane proteins with large hydrophilic domains achieved by the carbon sandwich preparation dramatically improves the resolution compared with single carbon support film preparation. We also provide updated statistics for the data collection required to determine previously published structures that were based on samples extremely susceptible to beam-induced image shift. Further improvement of the carbon sandwich preparation with highly reproducible preservation of 2D crystals is desired for more efficient data collection, which is indispensable for high-resolution structural analysis of fragile membrane proteins by electron crystallography.

CHAPTER 4

Three-dimensional structure of H^+,K^+-ATPase in the *E1* state

4.1. Summary

Gastric H^+,K^+-ATPase uses ATP to pump protons across the gastric membrane. Its active transport is achieved by cyclical conformational changes between two principal reaction states, *E1* and *E2*, and their respective auto-phosphorylated form, *E1*P and *E2*P. Although cryo-EM structures of gastric H^+,K^+-ATPase in *E2*P and its transition states provide important structural information relevant to its physiological functions, structure of other principal reaction states are so far missing. Here we show the first three-dimensional structure of H^+,K^+-ATPase in the *E1* state analyzed at 14Å resolution, employing electron crystallography of two-dimensional crystals. As crystals were grown in the acidic condition (below pH 4) without any inhibitors or ligands, the H^+,K^+-ATPase molecules in the crystals are likely to be accumulated in the H^+-bound *E1* state. To our surprise, the conformation of the cytoplasmic domains, especially P and N domains, showed compact configuration in the EM map of H^+,K^+-ATPase *E1* state compared with that of *E2*P state. This structural feature is in marked contrast to the widely opened N-domain found in the X-ray structure of SERCA *E1* state. Measurement of fluorescence intensity derived from H^+,K^+-ATPase labeled with fluorescein 5'- isothiocyanate (FITC) suggested hydrophobic environment of ATP-binding site (FITC bound to Lys518) at the N domain of H^+,K^+-ATPase *E1* state, thus most likely that the N domain is in close proximity to the P domain in the solution at the *E1* state. Observed close orientation between ATP- binding site and auto-phosphorylation site in the H^+,K^+-ATPase *E1* state might be helpful for the high-affinity ATP binding and subsequent phosphoryl transfer to the P domain, therefore providing an advantage on the efficient turnover of the vectorial cation transport achieved by H^+,K^+-ATPase, and probably P-type ATPase in general.

4.2. Introduction

Like other member of P-type ATPases, active transport of gastric H^+,K^+-ATPase is accomplished by cyclical conversion between two principal reaction states (*E1*, *E2*) and their corresponding auto-phosphorylated form (*E1*P, *E2*P) (see Chapter 1, Fig. 1.3. for details). Characteristic of all P-type ATPases, the transport cycle is accompanied by large conformational changes of the enzyme, which is well understood, in the case of best-studied SERCA, by its crystal structures in several of different reaction states (see Chapter 1, Fig. 1.5. for details). However, so far crystal structures of only one reaction state have been reported for Type P1B Cu^{2+}-ATPase [Gordon *et al.*, 2011]. Type P3 plant H^+-ATPase [Pedersen *et al.*, 2007], and two different reaction states (*E1*P-ADP and *E2*·P states) for Na^+,K^+-ATPase [Kanai *et al.*, 2013; Morth *et al.*, 2007] have been reported for other P-type ATPase members. Therefore, a series of structural analysis in different states of the transport cycle using a same target protein is required to understand common conformational changes conserved among P-type ATPases, *vice versa*, to identify unique mechanisms specific for each P-type ATPases.

Previously, our group reported several unique mechanisms of gastric H^+,K^+-ATPase relevant to its physiological functions [Abe *et al.*, 2009; Abe *et al.*, 2010; Abe *et al.*, 2012], based on the three-dimensional structures determined by electron crystallography in combination with functional studies. Furthermore, conformational changes similar to SERCA have been identified by the determination of a drug-bound structure [Abe *et al.*, 2011]. These structural analyses are, however, limited to *E2*P state and the transition states of its dephosphorylation, thus structural information of other principle reaction states are prerequisite for understanding conformational conversion of the H^+,K^+-ATPase during its transport cycle.

The structure of H^+,K^+-ATPase in the *E1* state is of special interest, as this conformation accept protons and ATP to initiate the transport cycle. Although X-ray structure of SERCA in the Ca^{2+}-bound *E1* state have been reported as the first X-ray structure of P-type ATPase [Toyoshima *et al.*, 2000], its N domain is largely separated from the P domain, and thus ATP-binding site is totally exposed to the bulk solution (so-called open conformation). Since such an open conformation of the N domain is hardly found in any other crystal structures of SERCA or other P-type ATPases so far reported, it is still controversial whether the structure of SERCA in the *E1* state is indeed open or should in fact be closed. Also, it is elusive whether SERCA-like open conformation can commonly be applied for the *E1* state of H^+,K^+-ATPase and other

Table 4.1. Part of 2D crystal screening parameters

Parameters with underline were applied for the 2D crystal formation used for the structural analysis

Parameters		effect	Parameters		effect	Parameters		effect
pH	3.7	x	Additives	glycerol	++ (40%)	Temp	on ice	+
	3.9	++		sucroce	x (40%)		4 C	-
	4.0	++		PEG400	x (40%)		20 C	x
	4.1	+		trehalose	x (40%)	Dialysis membrane (MWCO)	8,000	X
	4.5	x		hydroquinone	+		25,000	+
Buffer	acetate	+		DTT	+		50,000	-
	propionate	++	Detergent	DM	--		100,000	x
	butylate	+		UDM	x	Buffer change	3days x 1	x
	valerate	+		OTG	x		1day x 3	-
	MES	x		C12E8	x		12 h x 4	+
	citrate	x	Phopholipid	DOPC	--		6h x 8	-
Cation	Na	x		DOPS	x	Buffer volume	1L	+
	Li	x		egg PC	x		300 mL	+
	Mg	++(1mM)		E. coli total lipid	x		50 mL	--
	Mg	--(5 mM)		Egg SM	-		5 mL	x
				Brain SM	+			
				DOSM	++			
				cholesterol	x			

++, significantly improved; +, improved; -, no effect; --, negative effect; x, no crystals obtained.
Abbreviations: PEG, polyethylene glycol; DM, decyl maltoside, UDM, undecyl maltoside; OTG, octyl thioglucoside; DOPC, dioleoyl phosphatydilcholine; DOPS, dioleoyl phosphatidylserine; SM, sphingomyelin.

Table 4.2. Purified membrane fractions and 2D crystal qualities

Lot #, fraction	Specific activity (μmol/mg/h)[1]	LPR (w/w)[2]	Frequency[3]	Quality[4]
0630, G1 f2*	397	1.1	++	++
0903, G1 f2	527	1.2	+	++
0116, G1 f2	408	1.3	+	+
0409, G1 f3	477	0.9	+	-
1207, G1 f3*	434	1	++	++
0903, G1 f3	673	1	++	+
0908, G1 f3	595	1.1	-	-
0906, G2 f2	245	1.2	- -	- -

[1]Specific H^+,K^+-ATPase activity of indicated membrane fractions.
[2]Lipid-to-protein ratio of membrane fractions.
[3]Frequency of 2D crystals from indicated lot of the membrane fractions, observed in their negatively stained specimen.
[4]Quality of 2D crystals formed from each membrane lot, as determined by FFT of negatively stained 2D crystals.
*Membrane fractions used for the structural analysis.

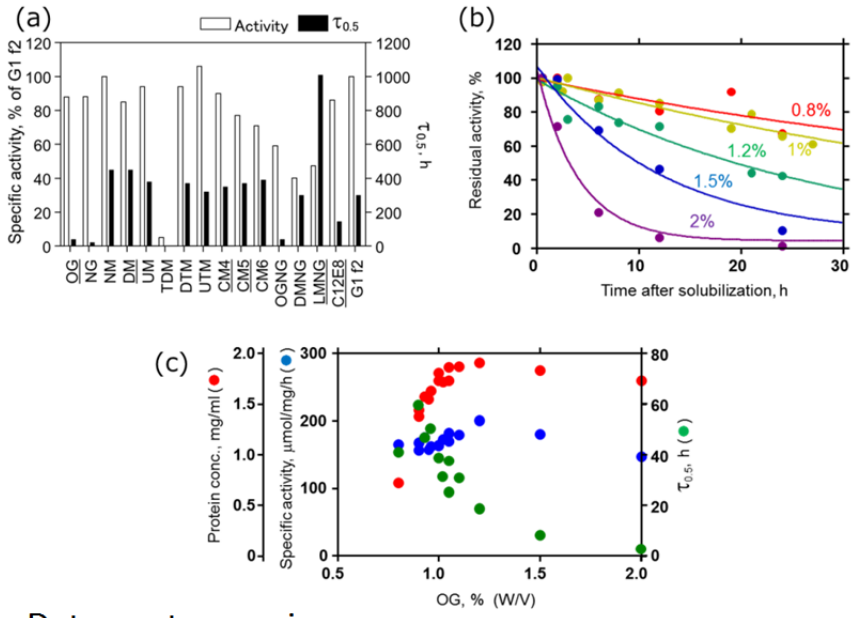

Fig. 4.1. Detergent screenings

(a) Membrane-bound H^+,K^+-ATPase was solubilized with indicated detergent, and their specific ATPase activity was measured (open column). The ATPase activity of membrane-bound preparation (G1 f2) set as 100%. After solubilization, they were stored at 4 ºC, and residual activities were followed to estimate half-life ($\tau_{0.5}$, closed column) which gave the activity of half maximum. Detergents with underline indicate those used for the 2D crystallization (mostly in *E2*P analogue states). It is notable that, except OG, no detergent gave 2D crystals in the *E1* state so far examined. Abbreviations used: NG, nonyl glucoside; NM, nonyl maltoside; UM, undecyl maltoside; TDM, tetradecyl maltoside; DTM, decyl thiomaltocide; UTM, undecyl thiomaltoside; CM4, cymal-4; CM5, cymal-5; CM6, cymal-6; OGNG, octyl glucose neopentyl glycol; DMNG, decyl maltoside neopentyl glycol ; LMNG, lauryl maltoside neopentyl glycol. (b) Time course of the residual ATPase activities after OG-solubilization. Solubilized supernatant with various concentrations of OG (0.8-2%, as indicated in the figure) were kept on ice, and aliquots were removed at various time to measure ATPase activity. Plotted values were percent of specific ATPase activity just after solubilization. Data were fitted in single exponential function and estimated their half-life ($\tau_{0.5}$) which is shown in panel c. (c) Dose dependence of OG. Protein concentrations (red circles) and specific activities just after solubilization (blue circles) in the supernatant and its half-life (green circles) were plotted as function of OG concentration. In these experiments, the ATPase activity was measured at pH 5.5, 37 ºC, thus specific activity of the membrane fraction is 211 μmol/mg/h.

P-type ATPase in general.

In this chapter, we show the first 3D structure of H^+,K^+-ATPase in the ligand-free, *E1* state analyzed at 14Å resolution. Compared with the structure of SERCA, we discuss conservations and differences between these two P-type ATPases.

4.3. Results and discussion

4.3.1. Two-dimensional crystallization trials

Our group previously reported that octylglucoside (OG)-solubilized H^+,K^+-ATPase forms tubular crystals at the acidic pH of around 4.0 [Nishizawa *et al.*, 2008]. To

improve 2D crystal quality, various crystallization conditions have been screened, including detergent, pH, additives, phospholipids, dialysis parameters and other coditions (Table 4.1.). Except OG, none of other detergent produced 2D crystals so far in the absence of inhibitor or ligand at the acidic pH (*i.e.*, condition favorable to *E1* state), despite of low stability of OG-solubilized H^+,K^+-ATPase ($\tau_{0.5}$ = 40 h) (Fig. 4.1.a). Because the stability of the ATPase activity is highly dependent on OG concentrations (Fig. 4.1.b,c), crystals were only produced in the OG concentrations ranging 0.8%-1.1%. Due to this instability of OG-solubilized H^+,K^+-ATPase, low temperature (on ice) and fast removal of OG from the solubilized samples by dialysis (exchange dialysis buffer 4 times against 100 mL detergent-free solutions) is important for the crystal production (Table 4.1).

Besides solution conditions, we found that the population and quality of 2D crystals were variable among several different lot of purified membrane fractions (Table 4.2). Because *E1* crystals can be formed without exogenously added phospholipid, amount and/or composition of endogenous lipid may be critical for the crystal formation. In fact, addition of small amount (LPR of below 0.1) of dioleoyl sphingomyelin (DOSM), which is found unusually high content (around 20% of total phospholipid) in the purified pig gastric membrane [Sen *et al.*, 1979], improved crystal quality. Incorporation of suitable amount of sphingomyelin may have an effect of infilling gaps between neighboring H^+,K^+-ATPase molecules reconstituted in the lipid bilayer, or it may simply bind to the hydrophobic part of the enzyme.

High concentration of glycerol (40%) was important for the activity preservation, and thus required for the crystal production. We further found that its removal prior to EM

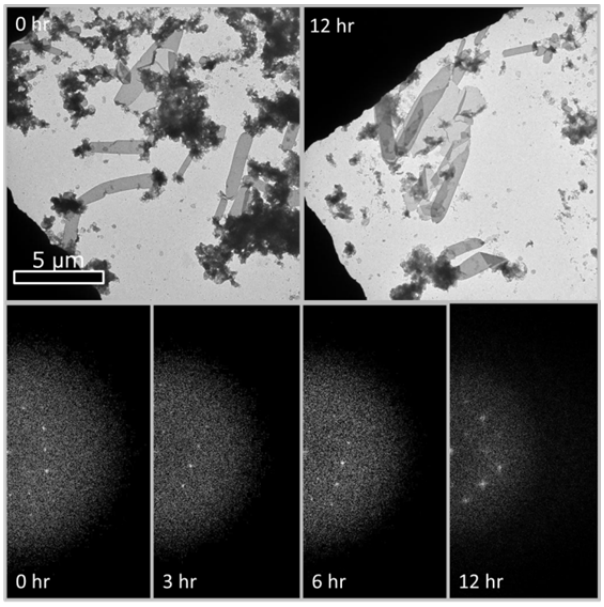

Fig. 4.2. Time course after glycerol removal

After dialysis for 2.5 days with 40% glycerol buffer, dialysis buttons were moved to the glycerol-free buffer for 3 h to remove glycerol form the crystal samples (see Materials and Methods for details). Crystal samples were then taken from dialysis buttons, kept on ice, and negatively stained at indicated time (0-12 hour). Lower panels show representatives of Fourier transform of negatively-stained 2D crystals (in this case single-layered crystals) found in the sample stained at indicated time. Broaden diffraction spots found in 12 h sample indicate crystal disorder, although their crystal morphologies were similar (upper panels).

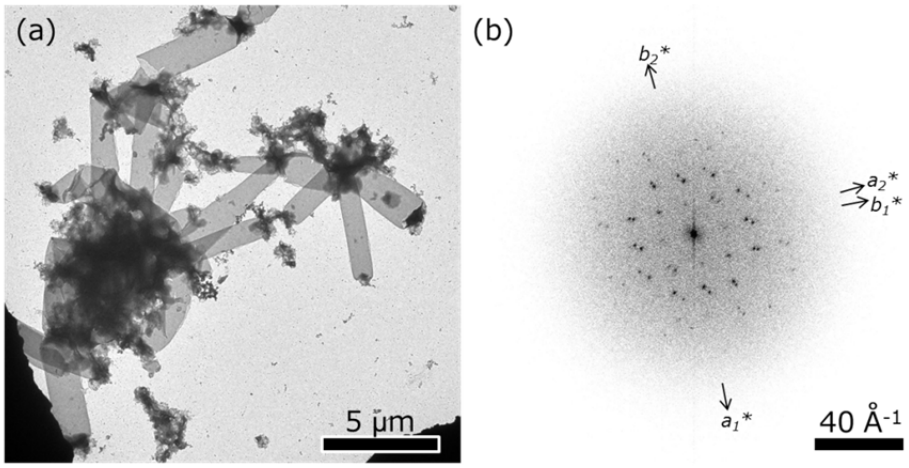

Fig. 4.3. 2D crystals used for the structural analysis

Tubular 2D crystals were frequently obtained in the refined crystallization conditions (a). The Fourier transformation of the crystal image (b) reveals two sets of diffraction spots that originated from upper and lower layer of the flattened tubular 2D crystals.

observation improves crystal quality. However, due to low concentration of glycerol in the crystalline samples, crystals are instable and their qualities become gradually worse after glycerol removal (Fig. 4.2.). Therefore, all the crystals used for the structural analysis were prepared within 6 h after glycerol removal.

As described, parameters of 2D crystallization were refined, and now we were able to produce larger 2D tubular crystals with higher populations and qualities (Fig. 4.3), compared to the previous situation [Nishizawa *et al.*, 2008]. Except H^+ (low pH), this crystallization condition does not contain any factor driving the H^+,K^+-ATPase in a particular conformation, such as analogues of ATP or phosphate, specific inhibitors and transport substrates, thus H^+,K^+-ATPases in the crystals are expected to be in the *E1* state. This notion was supported by limited proteolysis study (Fig. 4.4.). The membrane-bound H^+,K^+-ATPase in solution similar to 2D crystallization condition (*i.e.*,

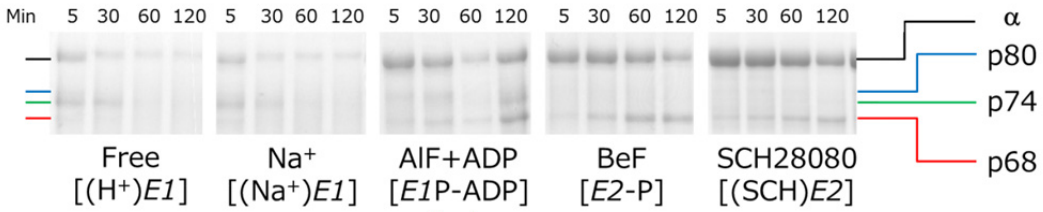

Fig. 4.4. Trypsin digestion of H^+,K^+-ATPase

Purified membrane fractions in the absence (Free) or presence of the indicated ligands (see Material and Methods for details) were incubated with trypsin at a pH 5.5. SDS-PAGE gels of the resulting tryptic fragments were shown. The position of the α-subunit of H^+,K^+-ATPase and its digestion fragments are indicated on the right. Fragment of p74 is accumulated at 5-30 min in the "Free" and "Na^+" conditions, whereas others showed digestion patterns distinguishable from those of *E1* state conditions.

ligand-free, pH 5.5) showed digestion patterns distinguishable from those of *E1*P-ADP, *E2*P or (SCH)*E2* states [Nishizawa *et al.*, 2008]. Digestion patterns of the ligand-free condition did not change in the presence of high concentration of Na^+, which is reported to act as a surrogate of H^+ and drives the enzyme into the *E1* state [Rabon *et al.*, 1990]. The proteolysis experiment was performed in the pH 5.5, since the acidic pH of crystallization buffer (pH 3.9~4.0) inhibits the enzyme activity of trypsin. However, the higher H^+ concentration in the crystallization buffer would favor the expected *E1* state. About 70% of the specific ATPase activity remains in the 2D crystals after dialysis, suggesting that the proteins in the 2D crystals are still active and capable of binding of transport substrate (*i.e.*, H^+). These data suggest that H^+,K^+-ATPase molecules in 2D crystal is likely to be accumulated in the H^+-bound *E1* state.

4.3.2. Sample preparations and data analysis

Like other 2D crystals of H^+,K^+-ATPase in the *E2*P and its transition states, 2D crystals of *E1* state were also sensitive to dehydration and accompanied change in concentrations of reagents occurred during ice-embedding process, provably due to its crystal contact between hydrophilic domains (see chapter 3 for details). To prevent crystal distortion by the dehydration effect, they had been embedded in relatively thick ice using ordinary single carbon preparations for the data collection by cryo-EM. However, no single isotropic data could be obtained even from the 20º tilted specimen prepared by single carbon support film, because specimens with thick ice are severely affected by the image shift due to beam-induced specimen charging, and this charging effect is strongly emphasized in the tilted specimen (*e.g.*, see Chapter 3, Table 3.1). This is one of the reasons why data collection from *E1* crystals was limited only for the non-tilted specimen [Nishizawa *et al.*, 2008]. Dramatic improvement has been achieved by applying carbon sandwich technique for *E1* crystals. Its compensation effect for the charge-induced image shifts, and preservation effect of 2D crystal quality allows us to collect whole data set for the determination of 3D structure.

However, inherent quality of *E1* crystal is limited to 9~10Å even in the best case (Fig. 4.5 b, c), not comparable to those of other *E2*P crystals (6.5~8Å), even though refinement of crystallized conditions and sample preparation by carbon sandwich techniques have been applied. In most of the case, due to limited coherency of crystalline lattice and/or crystal curvature derived from their tubular morphology, the diffraction spots in Fourier transformation of the cryo-images were limited to ~20Å resolution (Fig. 4.5d).

Table 4.3. Electron crystallographic data

Two-dimensional crystal	
Space group	$P22_12_1$
Lattice constants (Å)	a = 129.8 Å, b = 117.0 Å,
	c = 360 Å (assumed), γ = 90°
Number of images (Total)	155
Tilt 0°	9
20°	18
45°	128
Total number of observed reflections	8,296
Total number of unique reflections	417
Overall phase residuals (weighted IQ) [a]	55.0 (41.9)
Defocus range (min – max)	8,103 – 25,349 Å
Resolution limit of merge data	14.0 Å

[a]Used reflections are better than IQ 6.

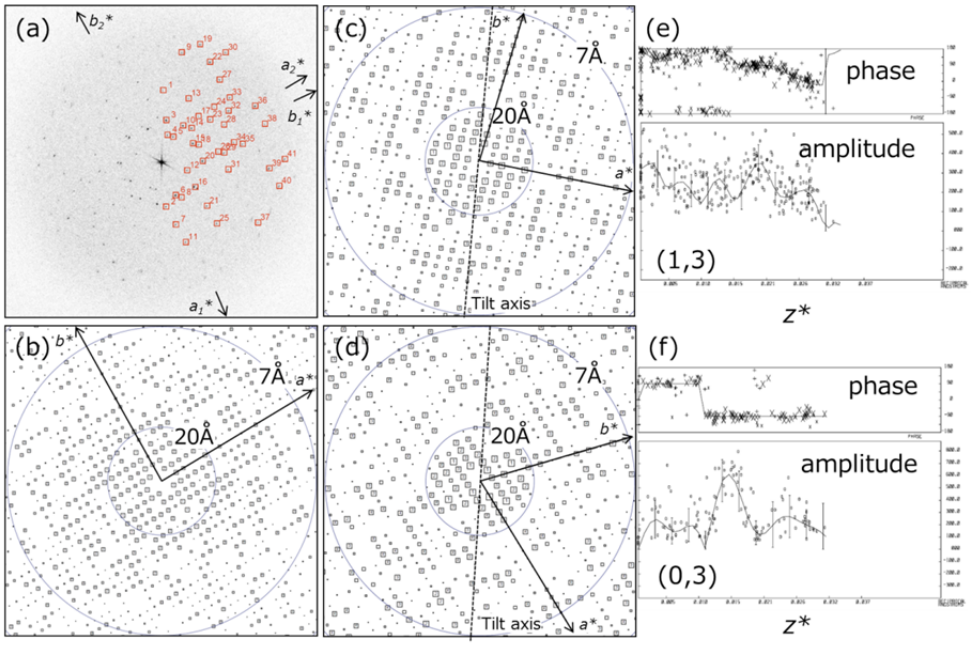

Fig. 4.5. Cryo-EM data of *E1* crystals prepared by carbon sandwich

(a) Fourier transformation of the tubular 2D crystals prepared by carbon sandwich technique. (b-d) IQ-plots [Henderson et al, JMB] of analyzed crystal images of non-tilted (b) or 45 tilted (c,d) specimen. (e,f) representative lattice lines from the 3D data set. The phase (upper panels) and amplitude (lower panel) data of (1,3) lattice line (e) and those of (0,3) lattice line.

To exclude poorly ordered crystal images from the 3D data set, structural factors were merged to 14Å according to their phase residuals, and the final EM density map was calculated at 14Å resolution to build a reliable structure (Table 4.3., Fig. 4.5e,f).

4.3.3. Cryo-EM structure of H^+,K^+-ATPase in the *E1* state.

As expected from similar tubular morphology of *E1* and *E2*P crystals, molecular packing of *E1* crystal is essentially the same to that of *E2*P crystals (Fig. 4.6). One layer of the crystalline membrane consists of two membrane layers, and are 360Å thick, although two crystalline layers always overlapped in the projection images of the tubular crystals (Fig. 4.3, 4.5a). The asymmetric unit contains one H^+,K^+-ATPase αβ-protomer, and αβ-protomers in the two-membrane layers are related to each other by a two-fold screw axis. An αβ-protomers in the same membrane do not form direct interaction, so that all crystal contacts are mediates by the cytoplasmic domains of protomers in adjoining membranes, with the luminal portion of the protomers (β-subunit ecto domain) protruding from the outer surface of the crystals (Fig. 4.6).

In the EM map of H^+,K^+-ATPase *E1* state (Fig. 4.7), overall structure of the cytoplasmic domains (A,P and N domains) shows compact configuration, although the individual domains are not completely resolved due to limited resolution of the structure. Fitting of the homology model derived from X-ray structure of Na^+,K^+-ATPase in the *E1*P-ADP state [Kanai *et al.*, 2013] to the EM map allows us to interpret the structural organization of the H^+,K^+-ATPase in the *E1* state (see Materials and Methods for details).

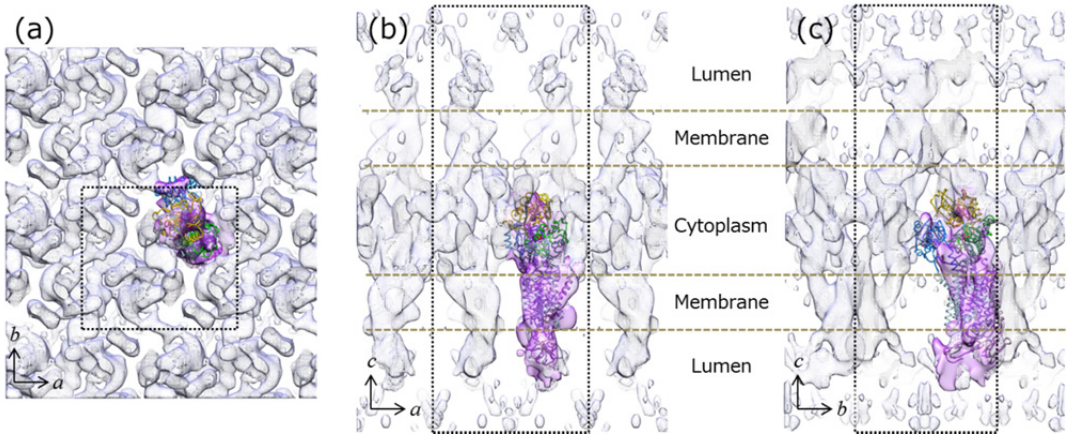

Fig. 4.6. Crystal packing

The density map of the H^+,K^+-ATPase 2D crystal contoured at 1 σ, viewed from indicated planes (a-c) shows that the 2D crystals consist of two membrane layer (indicated by wheat dotted lines). Asymmetric unit (*i.e.*, αβ-protomer of H^+,K^+-ATPase) is shown as magenta with superimposed homology model.

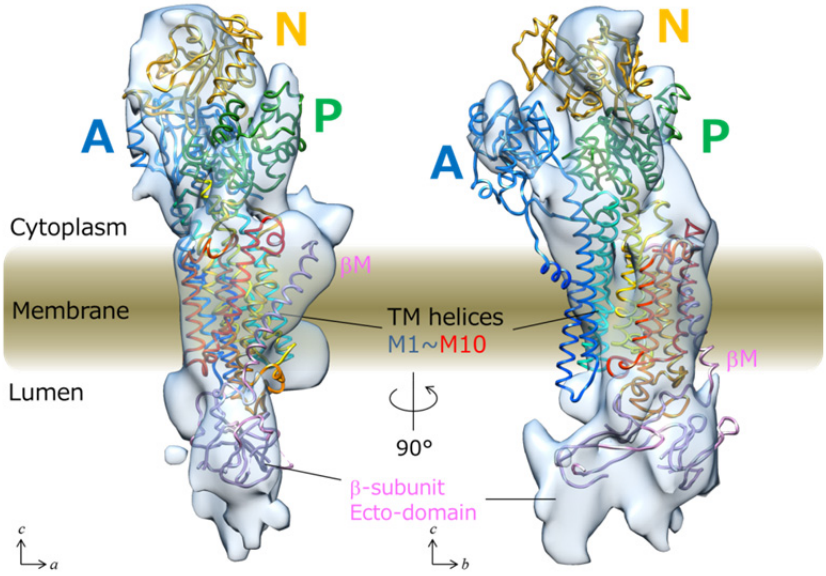

Fig. 4.7. Cryo-EM structure of H^+,K^+-ATPase in the *E1* state

Surface (light blue) representation of the extracted density map of an H^+,K^+-ATPase αβ-protomer with fit homology model in ribbon representation. Color code of the homology model: A domain, blue; P domain, green; N domain, yellow; TM helices M1-M10 of the α-subunit, gradual change from M1 (blue) to M10 (red); β-subunit, pink. Wheat box indicate the probable position of the lipid bilayer with total thickness of approximately 35Å. Crystal axes are indicated in lower left to show the view point of each structure.

4.3.4. Comparison between *E1* and *E2*P states of H^+,K^+-ATPase

Comparison of EM maps between *E1* and *E2*P states of H^+,K^+-ATPase reveals that the conformation of transmembrane (TM) helices M7-M10 and that of β-subunit (βM) in the *E1* state appeared to be similar to those in *E2*P state (Fig. 4.8a), good agreement with their least variations in the crystal structures of SERCA in different functional states, and proposed their anchoring property in the lipid bilayer [Abe *et al.*, 2010; Toyoshima, 2009]. In contrast, the density responsible for M1, M2 and connecting A domain in the EM map of *E1* state appeared to be sparse, probably reflects their flexibility (Fig. 4.8a). In the ligand-free *E1* state, auto-phosphorylation site (Fig. 4.8b, Asp385) at the center of the P domain must be empty. Thus, TGES motif which is located outermost of the A domain and covers phosphate (or its analogues) bound to the Asp385 in *E2*P state to prevent its spontaneous dephosphorylation [Toyoshima *et al.*, 2007], may not have particular interaction to the P domain in the *E1* state. This might be a reason why the A domain and connecting M1 and M2 are disordered. This flexibility may also be related to the fact that *E1* state is not H^+-occluded, but H^+-bound state. Since the cytoplasmic gate is proposed to be formed in between cytoplasmic

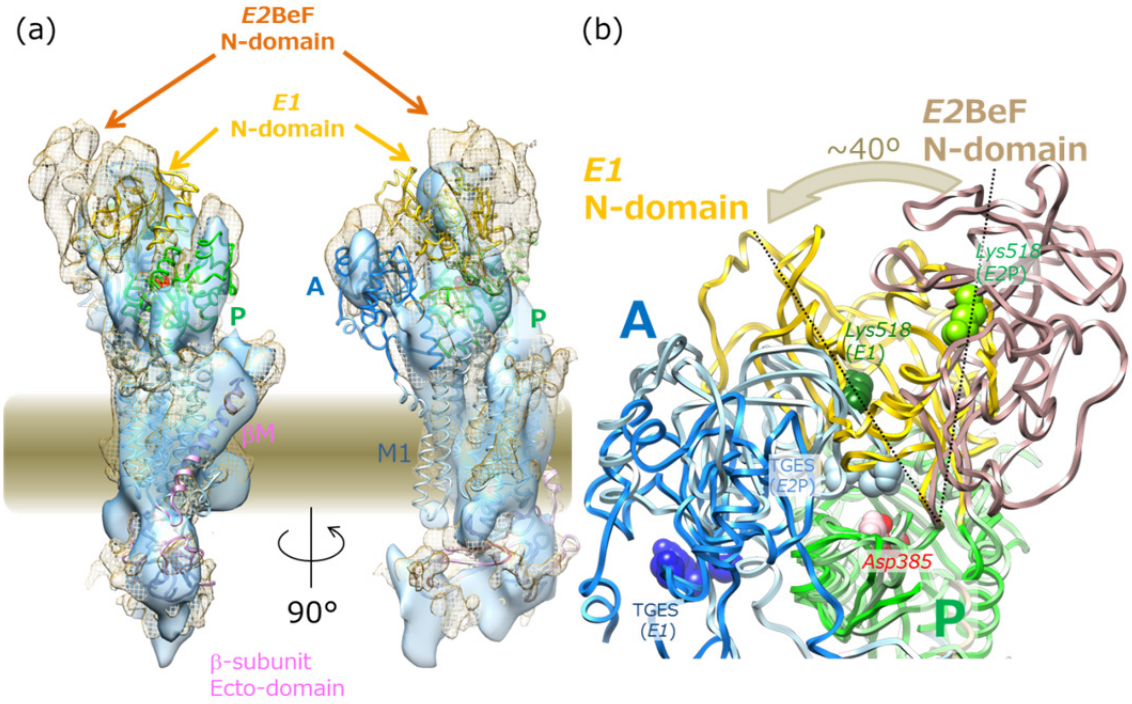

Fig. 4.8. Conformational difference between *E1* and *E2*P

(a) The surface (light blue) shows the EM map of H^+,K^+-ATPase *E1* with its homology model superimposed (color codes as in Fig. 4.9 except TM helices shown in light blue). Yellow mesh represents the EM map of H^+,K^+-ATPase *E2*P [Abe *et al.*, 2011]. (b) Comparison of homology models for H^+,K^+-ATPase *E1* (A domain, blue; P domain, green; N domain, yellow) and *E2*P (A domain, light blue; P domain, light green; N domain, light brown). Several important residues are indicated in the figure with sphere representations. Dotted lines indicate azimuthal positions of the N domain in each state, and wheat arrow indicates the movement of N domain during *E2*P to *E1* transition.

portion of M1 and M2, this part may form shielded, rigid structure when H^+ is occluded in the subsequent *E1*P state [Toyoshima *et al.*, 2004].

The most prominent structural difference between the *E1* and *E2*P states of H^+,K^+-ATPase can be found at their cytoplasmic portion (Fig. 4.8). The N domain of *E1* structure is closer, inclined ~40º toward the P domain compared with that of *E2*P structure (Fig. 4.8b). Because now in the *E1* state, TGES motif of the A domain is segregated from the P domain, this inclination of the N domain toward the phosphorylation site seems possible. As seen in the crystal packing of the *E1* structure (see *a*-*c* plane of the crystal in Fig 4.6), the length of the *a* axis mostly depends on the crystal contact at the top of N domain to the β-subunit N-terminus of the neighboring upside-down molecule related to two-fold screw symmetry. Thus large difference of the unit cell dimension in the direction of *a* axis between *E1* (129.8Å) and *E2*P related states (140-141Å) reflects observed conformational difference at the N domain.

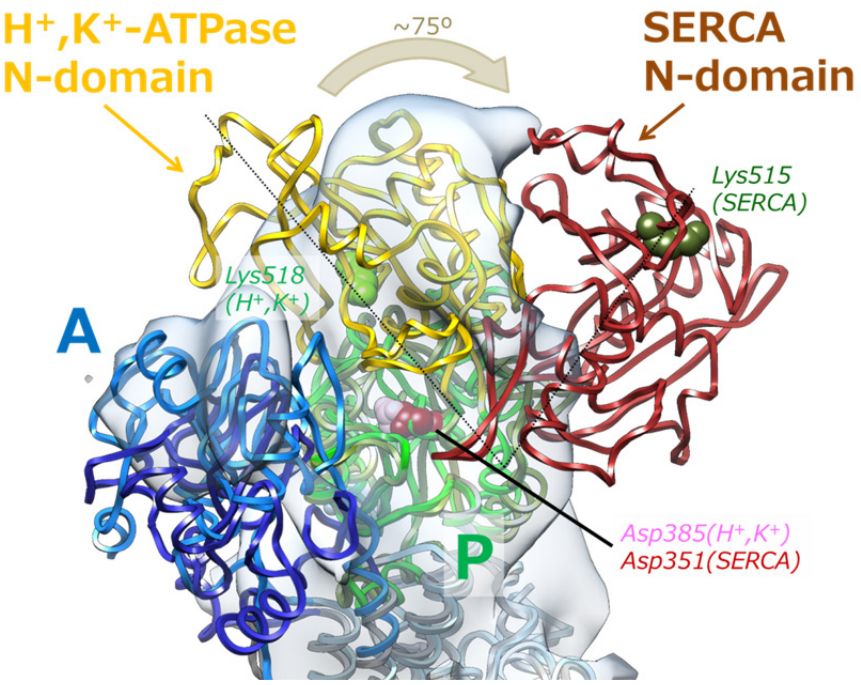

Fig. 4.9. Comparison between H^+,K^+-ATPase and SERCA in the *E1* state

Comparison of the H^+,K^+-ATPase in the *E1* state (light blue surface for EM density map with its homology model (color codes as in Fig. 4.8) superimposed), with X-ray structure of SERCA in the *E1* state (A domain, dark blue; P domain, dark green, N domain brown; pdb code: 1su4). Conserved Asp (pink for H^+,K^+-ATPase and red for SERCA) and Lys residues (light green for H^+,K^+-ATPase and dark green for SERCA) are indicated as spheres, to show approximate location of auto-phosphorylation site (Asp) and ATP-binding site (Lys), respectively. Wheat arrow indicates the different location of the N domain in each structure.

4.3.5. Difference between H^+,K^+-ATPase and SERCA in the *E1* state

The X-ray structure of SERCA in the *E1* state has shown specific conformation, notably the widely opened ATP-binding site located at the N domain (so-called open conformation, see Fig. 1.4a), which is distinct from any other structures of SERCA reported so far. In the present EM structure of H^+,K^+-ATPase in the *E1* state, however, location of the N domain is markedly different, showing more compact configuration than SERCA in the *E1* state (Fig. 4.9.). The N domain of H^+,K^+-ATPase in the *E1* state is inclined ~75° toward the P domain compared with that of SERCA *E1* state. We therefore confirmed whether the observed compact conformation of the P and N domain in H^+,K^+-ATPase *E1* structure is in fact occurred in the solution, or crystal condition and/or packing prevent their segregation in the 2D crystal, as described below.

4.3.6. FITC fluorescence measurement

A fluorescence probe fluorescein 5'-isothiocyanate (FITC) preferentially forms a covalent bond to ε-amino group of Lys-518 residue which is embedded in the conserved ^{518}KGAP ATP binding motif at the N domain [Farley and Faller, 1985]. This chemical modification of Lys residue impair H^+,K^+-ATPase activity due to loss of ATP-binding ability, suggesting FITC probe is located at the nucleotide-binding position. However, as FITC-modified H^+,K^+-ATPase can hydrolyze substrates less bulky than ATP such as acetyl phosphate or *p*-nitrophenyl phosphate (*p*NPP) [Abe *et al.*, 2005], FITC-modified enzyme is still active and undergoes conformational change in response to substrate binding, and therefore we could monitor conformational changes, especially those occurred in the N domain, by monitoring its fluorescence intensity [Rabon *et al.*, 1990].

Fluorinated phosphate analogues can mimic bound phosphate to the P domain, and drive the enzyme into *E2*P or its transition states [Danko *et al.*, 2004; Abe *et al.*, 2010]. We found that the addition of beryllium fluoride (BeF, induces close analogue of *E2*P ground state, *E2*-BeF) increase FITC fluorescence signal (Fig. 4.10a). In contrast, magnesium fluoride (MgF, analogue of transition state of *E2*P dephosphorylation, *E2*·P) decrease it (Fig. 4.10a). In the EM map of *E2*-BeF state (shown as mesh in Fig. 4.10), N domain is close to the A domain, and a density responsible for bound ADP can clearly be seen in between these two domains. In contrast, no density is observed at the position of ADP in the *E2*·MgF structure (shown as surface in Fig 4.10b), despite of its presence in the crystallization buffer of both states [Abe K., unpublished data]. Since bound ADP is likely to be coordinated by the outermost of the A domain in the *E2*-BeF structure, the presence or absence of ADP density in these EM structures of *E2*-BeF and *E2*·MgF would be related to their difference in distance between A and N domain (Fig. 4.10). When these two domains are in close position like *E2*-BeF structure, bound FITC located at the nucleotide binding site would also be surrounded by outermost amino acids of the A domain just like bound ADP does. Accordingly, FITC might be in the hydrophobic environment in which its fluorescence intensity is increased (Fig. 4.10a, "BeF" column). In the *E2*·MgF structure, however, the N domain is swayed from the A domain, and FITC may be exposed to the bulk solution which induces quenching of the fluorescence signal due to the hydrophilic environment of bound FITC (Fig. 4.10a, "MgF" column) [Abe K., unpublished data].

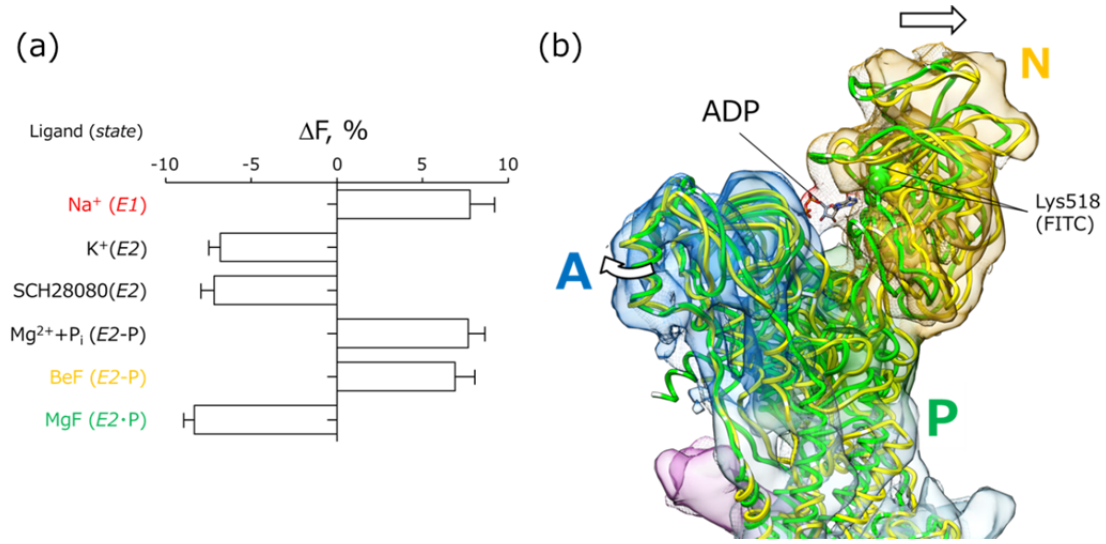

Fig. 4.10. Conformational change of H^+,K^+-ATPase monitored by FITC fluorescence

(a) FITC-modified H^+,K^+-ATPase membrane fractions were incubated at 37°C, pH 7.0, and their fluorescence intensity changes (ΔF) were monitored after addition of indicated reagents. Initial fluorescence intensity was set as 100%. Expected reaction states by the addition of indicated reagents were shown in parenthesis. (b) Structural description of opposite FITC fluorescence signals induced by BeF and MgF. Cryo-EM structure of *E2*·MgF (surface) and *E2*-BeF (mesh) are shown with superimposed their respective homology models (yellow and green ribbons, respectively). A, P and N domains are shown as blue, green and yellow, respectively, in each EM map. Bound ADP in the *E2*-BeF structure, but missing in the *E2*·MgF structure, is shown as stick representation. FITC-binding site (Lys518) is shown as spheres in each map. White arrows indicate conformational change observed during *E2*-BeF to *E2*·MgF state. EM maps in this figure are based on the unpublished data from K. Abe.

When Na^+ is added to the FITC-bound enzyme, its fluorescence signal is increased (Fig. 4.10a, "Na^+" column). As Na^+ act as a surrogate of H^+, drives the enzyme into the *E1* state [Rabon *et al.*, 1990], observed increase in fluorescence signal suggests hydrophobic environment of bound FITC in the *E1* state. Such fluorescence change would not occur if the *E1* state of H^+,K^+-ATPase took an open conformation like SERCA *E1* structure, in which ATP-binding site is totally exposed to the bulk solution (see Fig. 4.9, Lys515 in the SERCA model). Therefore, we conclude that the close proximity between the P and N domain (see Fig. 4.9, Asp385 and Lys518 in H^+,K^+-ATPase model) observed in the structure of H^+,K^+-ATPase in the *E1* state is consistent with FITC fluorescence study, thus also taking place for the membrane bound enzyme in the solution.

4.3.7. Implications for the compact headpiece in the cytoplasmic domains of H^+,K^+-ATPase in the *E1* state

A remarkable feature of SRECA is that the cytoplasmic domains adopt a compact conformation in all functional states with the sole exception of the structure of the *E1* state with bound Ca^{2+} in the absence of ATP, in which case the cytoplasmic domains adopt an open conformation. It is therefore still controversial whether the structure of SERCA in the *E1* state is indeed open or should in fact be closed at the physiological conditions. In our cryo-EM structure of H^+,K^+-ATPase in the *E1* state, the N domain is in close proximity to the P domain in the crystal, which is corroborated by FITC fluorescence experiment in the solution. Therefore, it is unlikely that the H^+,K^+-ATPase undergoes large conformational change like what SERCA does. An analysis of 3D microcrystals of SERCA in the *E1* state showed that the crystals had variable unit cell dimensions, especially in the direction of the *c*-axis [Ogawa *et al.*, 1998; Sheong *et al.*, 1996], suggesting that the N domain is flexible and can possibly be in either an open and a compact conformation in the *E1* state. Recently reported FRET analysis using SERCA with fluorescence fusion proteins (2-color SERCA) suggests closure of the cytoplasmic headpiece with Ca^{2+}-binding (*i.e.*, (Ca^{2+})*E1* state) [Hou *et al.*, 2012]. These observations suggest that widely opened conformation of SERCA in the *E1* state is possible, but is not feasible when turn over its transport cycle under physiological situation.

It is not surprising that the relative orientation of the cytoplasmic domains differs among P-type ATPases. Indeed, different orientations of the A and N domain in the *E2*P state have been reported for H^+,K^+-ATPase [Abe *et al.*, 2010], and also for Na^+,K^+-ATPase and SERCA [Liu *et al.*, 2009; Shinoda *et al.*, 2009]. These differences contribute to the susceptibility of bound phosphate analogues in the former case [Abe *et al.*, 2010], and is a determinant of the modulatory ATP effect which accelerate *E2*P dephosphorylation in the latter case [Liu *et al.*, 2009]. Therefore, besides their cation selectivity, amino acids at the interface of each cytoplasmic domain might contribute to the unique properties of each P-type ATPases.

The important structural implication for ATP affinity is the number of salt bridges formed between the ATP molecule and the P/N domains. In the SERCA structure of the *E1*P-ADP state, not only N domain but also P domain makes contacts with ATP (Fig. 4.11a) to achieve its high affinity binding (range of micromolar). In contrast, bound ATP is coordinated mostly by the N domain, only few residues from the P domain are involved in ATP binding in the *E2* state, in which the affinity of ATP is low (range of millimolar) [Jensen *et al.*, 2006]. This may be a reason why H^+,K^+-ATPase adopts a compact conformation in its *E1* state. The *E1* state is defined as high affinity for H^+ as well as ATP to initiate auto-phosphorylation, compact configuration of the P and N

domains in the H^+,K^+-ATPase *E1* state satisfies a requirement for the high-affinity ATP binding (Fig. 4.11a). Therefore, we suspect that the affinity for ATP in an open conformation like SERCA *E1* state is likely to be low, as bound ATP at the N domain is too distant to be coordinated by amino acids in the P domain if ATP would bind to the N domain (Fig. 4.11b). For high-affinity ATP binding and subsequent auto-phosphorylation, appropriately formed ATP binding site inbetween N and P domain provides large benefit for the efficient turnover of the transport cycle achieved by H^+,K^+-ATPase, and probably most of other P-type ATPases in general.

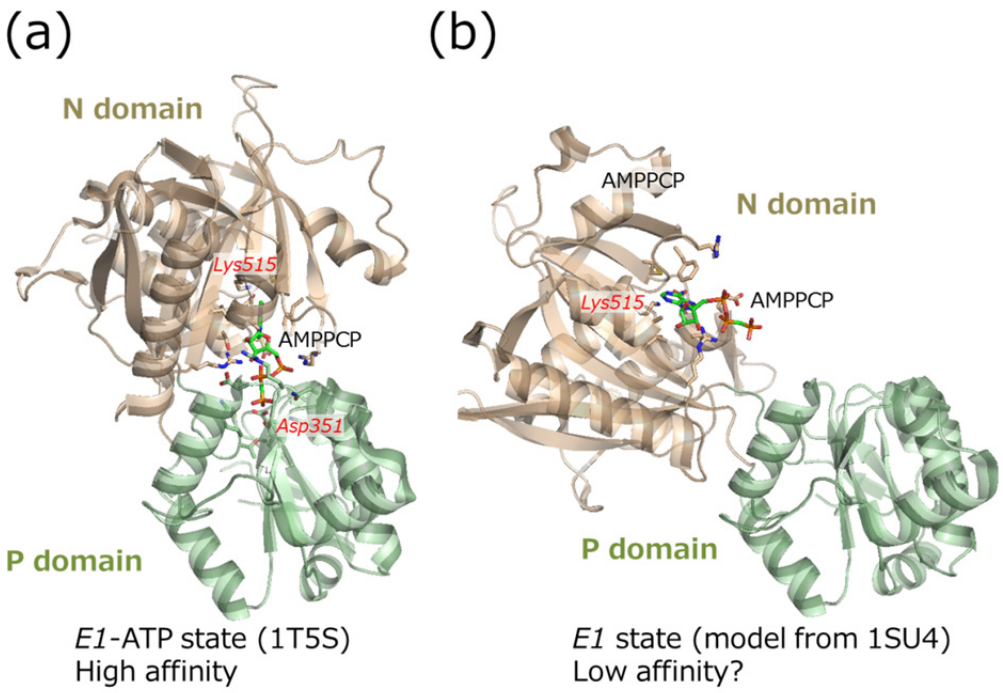

Fig. 4.11. Bound AMP-PCP in the *E1*-ATP or *E1* state of SERCA

(a) An atomic model of SERCA in the *E1*-ATP state (pdb code, 1T5S) with bound AMP-PCP (non-hydrolyzable analogue of ATP, stick), which is coordinated amino acid residues from P and N domain (shown as sticks). (b) A model of ATP-binding in the *E1* state of SERCA (pdb code, 1SU4). AMP-PCP is fit to the *E1* model according to the coordinating residues at the N domain in the *E1*-ATP structure (a). Positions of Asp351 (phosphorylation site) and Lys515 (ATP-binding motif) are indicated in the figure. Only P (green ribbons) and N (wheat ribbons) are extracted from each structures for simplicity.

CHAPTER 5

Conclusions and perspectives

5. Conclusions and perspectives

The research presented in this thesis has provided the first 3D structure of gastric H^+,K^+-ATPase in the *E1* state, and thus novel insights into the conformational change during its transport cycle, as briefly outlined bellow.

It was demonstrated that the N domain of the H^+,K^+-ATPase *E1* state is in the closed conformation, which is marked contrast to the open conformation reported in the first X-ray structure of SERCA *E1* state. Fluorescence study probed by FITC bound to the ATP-binding site at the N domain of H^+,K^+-ATPase suggests relatively hydrophobic environment of ATP-binding site, corroborating that N and P domain is in close proximity in the H^+,K^+-ATPase *E1* state in the solution. Accordingly, it was concluded that the observed closed conformation is feasible, as ATP-binding and subsequent phosphoryl transfer requires high-affinity ATP binding site coordinated by both of N and P domains, thus also taking place when H^+,K^+-ATPase is turning over under the physiological situation.

Our conclusion also provides an example for the long standing debate of whether the structure of P-type ATPases in the *E1* state is indeed open or should in fact be closed. Because high-affinity ATP-binding is essential requirement for the *E1* state in all P-type ATPases, observed closed conformation in the cytoplasmic domain in the *E1* state of H^+,K^+-ATPase may also be applicable for other P-type ATPases in general.

It should be also mentioned that the carbon sandwich technique was indispensable in terms of data collection and crystal preservation for the structural determination achieved in this thesis. This technique could also be applied for the cryo-preparation of 2D crystals of other membrane proteins, to extract structural information in their full potential.

Gastric H^+,K^+-ATPase faces a highly demanding task of pumping protons against a million-fold gradient ranging from approximately pH 7 in the parietal cell to pH 1 in the stomach. Generation and maintaining a potent concentration gradient of six orders of magnitude is hardly met by any other pumps in nature. So far, cryo-EM structures of H^+,K^+-ATPase with medium resolution (6.5-8Å by our group, and 14Å in this study) provide important information based on the domain movement and helix arrangement in several different conformations. However, high resolution structural analysis corroborated with detailed functional studies are mandatory, to shed light on the molecular mechanism of how the energetic challenges that membrane pumps are confronted with are met in living system.

Acknowledgements

This thesis, and also the whole of my phD experience at the Kyoto University, is a result of the guidance and support of Prof. Yoshinori Fujiyoshi and Dr. Kazuhiro Abe. Not only have they provided me funds and fresh perspectives to explore in my research, but they have also guided and helped me out of the many problems that I have encountered either in research and life. Their patient guidance, insightful advice and considerate concern have granted me great encouragement and confidence to persist and finish my study.

I would like to express my sincere gratitude to Prof. Tomoko Doi and Prof. Yoshinori Shichida for being my supervisor of the Kyoto University from the 2nd year of phD experience and thesis committee. Their valuable suggestions and comments on my experiments and thesis were very helpful. I also appreciate very much Dr. Atunori Oshima to be my supervisor of Nagoya University from the 2nd year of phD experience and offer me various helps in Nagoya University.

I also would like to extend my appreciations to the many researchers, graduate students and colleagues who have helped me in various aspects of my research including Dr. Kazutoshi Tani, Ms. Tomomi Hotta, Ms. Mie Tanaka and all the other members in Prof. Fujiyoshi's group.

Finally, I want to thank my parents and relatives for the advice, love and support that have enriched my life. Thank you very much for trust me to make my own decisions and support them. These have allowed another degreed scientist to begin his career.

Bibliography

Abe, K., Kaya, S., Taniguchi, K., Hayashi, Y., Imagawa, T., Kikumoto, M., Oiwa, K. and Sakaguchi, K. (2005) Evidence for a relationship between activity and the tetraprotomeric assembly of solubilized pig gastric H/K-ATPase. *J. Biochem.*, **138**, 293-301.

Abe, K., Tani, K., Nishizawa, T. and Fujiyoshi, Y. (2009) Inter-subunit interaction of gastric H^+,K^+-ATPase prevents reverse reaction of the transport cycle. *EMBO J.*, **28**, 1637-1643.

Abe, K., Tani, K. and Fujiyoshi, Y. (2010) Structural and functional characterization of H^+,K^+-ATPase with bound fluorinated phosphate analogs. *J. Struct. Biol.*, **170**, 60-68.

Abe, K., Tani, K. and Fujiyoshi, Y. (2011) Conformational rearrangement of gastric H^+,K^+-ATPase induced by an acid suppressant. *Nat. Commun.*, **2**, 155.

Abe, K., Tani, K., Friedrich, T. and Fujiyoshi, Y. (2012) Cryo-EM structure of gastric H^+,K^+-ATPase with a single occupied cation-binding site. *Proc. Natl. Acad. Sci. USA.*, **109**, 18401-18406.

Abrahams, J.P., Leslie, A.G.W. and Walker, J.E. (1994) Structure at 2.8 Å resolution of F1-ATPase from bovine heart mitochondria. *Nature*, **370**, 621-628.

Agard, D.A. (1983) A least-squares method for determining structure factors in three-dimensional tilted-view reconstructions. *J. Mol. Biol.*, **167**, 849–852.

Amos, L.A., Henderson, R. and Unwin, N. (1982) Three-dimensional structure determination by electron microscopy of two-dimensional crystals. *Prog. Biophys. Mol. Biol.*, **39**, 183-231.

Argüello, J.M., Eren, E. and González-Guerrero, M. (2007) The structure and function of heavy metal transport P1B-ATPases. *Biometals*, **20**, 233-248.

Auer, M., Scarborough, G.A. and Kühlbrandt, W. (1998) Three-dimensional map of the plasma membrane H+-ATPase in the open conformation. *Nature*, **392**, 840-843.

Axelsen, K.B. and Palmgren, M.G. (1998) Evolution of substrate specificities in the P-type ATPase superfamily. *J. Mol. Evol.*, **46**, 84-101.

Bradley, D.E. in: D. Kay (Ed.), *Techniques for Electron Microscopy*. Blackwell,

Oxford, 58.

Bublitz, M., Poulsen, H., Morth, J.P. and Nissen, P. (2010) In and out of the cation pumps: P-type ATPase structure revisited. *Curr. Opin. Struct. Biol.*, **20**, 431-439.

Bublitz, M., Morth, J.P. and Nissen, P. (2011) P-type ATPases at a glance. *J. Cell Sci.*, **124**, 2515-2519.

Carilli, C.T., Farley, R.A., Perlman, D.M. and Cantley, L.C. (1982) The active site structure of Na^+- and K^+-stimulated ATPase. Location of a specific fluorescein isothiocyanate reactive site. *J. Biol. Chem.*, **257**, 5601-5606.

Chang G. and Roth C.B. (2001) Structure of MsbA from *E. coli*: a homolog of the multidrug resistance ATP binding cassette (ABC) transporters. *Science*, **293**, 1793-1800.

Chang, H., Saccomani, G., Rabon G., Schackmann, R. and Sachs, G. (1977) Proton transport by gastric membrane vesicles. *Biochim. Biophys. Acta.*, **464**, 313–327.

Cheong, G.W., Young, H.S., Ogawa, H., Toyoshima, C. and Stokes D.L. (1996) Lamellar stacking in three-dimensional crystals of Ca^{2+}-ATPase from sarcoplasmic reticulum. *Biophys. J.*, **70**, 1689–1699.

Chifflet, S., Torriglia, A., Chiesa, R. and Tolosa, S. (1988). A method for the determination of inorganic phosphate in the presence of labile organic phosphate and high concentrations of protein: application to lens ATPases. *Anal. Biochem.*, **168**, 1–4.

Chiu, P-L., Kelly, D.F. and Walz, T. (2011) The use of trehalose in the preparation of specimen for molecular electron microscopy. *Micron*, **42**, 762-772.

Chow, D.C. and Forte, J.G. (1995) Functional significance of the beta-subunit for heterodimeric P-type ATPases. *J. Exp. Biol.*, **198**, 1–17.

Crowther, R.A., Henderson, R. and Smith, J.M. (1996) MRC image processing programs. *J. Struct. Biol.*, **116**, 9-16.

Danko, S., Yamasaki, K., Daiho, T. and Suzuki, H. (2004) Distinct natures of beryllium fluoride-bound, aluminum fluoride-bound, and magnesium fluoride-bound stable analogues of an ADP-insensitive phospoenzyme intermediate of sarcoplasmic reticulum Ca^{2+}-ATPase. *J.Biol. Chem.*, **279**, 14991-14998.

Dubochet, J., Chang, J.J., Freeman, R., Lepault, J. and McDowall, A.W. (1982) Frozen aqueous suspensions. *Ultramicroscopy*, **10**, 55-61.

Epstein, W. and Kim, B.S. (1971) Potassium transport loci in *Escherichia coli* K-12. *J. Bacteriol.*, **108**, 639-644.

Farley, R.A. and Faller, L.D. (1985) The amino acid sequence of an active site peptide from the H,K-ATPase of gastric mucosa. *J. Biol. Chem.*, **260**, 3899-3901.

Fernandez, J.J., Sanjurjo, J.R. and Carazo, J.M. (1997) A spectral estimation approach to contrast transfer function detection in electron microscopy. *Ultramicroscopy*, **68**, 267-295.

Forte, J.G., Forte, T.M., Black, J.A., Okamoto, C. and Wolosin, J.M. (1983) Correlation of parietal cell structure and function. *J. Clin. Gastroenterol.*, **5**, 17–27.

Fujiyoshi, Y., Mizusaki, T., Morikawa, K., Yamagishi, H., Aoki, Y., Kihara, H., Harada, Y. (1991) Development of a superfluid helium stage for high-resolution electron microscopy. *Ultramicroscopy*, **38**, 241-251.

Fujiyoshi, Y. (1998) The structural study of membrane proteins by electron crystallography. *Adv. Biophys.*, **35**, 25–80.

Fujiyoshi, Y. (2011). Electron crystallography for structural and functional studies of membrane proteins. *J. Electron Microsc. (Tokyo)*, **60**, 149-159.

Ganser, A.L. and Forte, J.G. (1973) K^+-stimulated ATPase in purified microsomes of bullfrog oxynic cells. *Biochim. Biophys. Acta*, **307**, 169-180.

Glaeser, R.M., Downing, K., DeRosier, D., Chiu, W. and Frank, J. (2007) *Electron crystallography of biological macromolecules* (Oxford University Press, Oxford).

Gonen, T., Sliz, P., Kistler, J., Cheng, Y. and Walz, T. (2004) Aquaporin-0 membrane junctions reveal the structure of a closed water pore. *Nature*, **429**, 193-197.

Gonen, T., Cheng, Y., Sliz, P., Hiroaki, Y., Fujiyoshi, Y., Harrison, S.C. and Walz, T. (2005) Lipid-protein interaction in double-layered two-dimensional AQP0 crystals. *Nature*, **438**, 633-638.

Gourdon, P., Liu, X.Y., Skjørringe, T., Morth, J.P., Møller, L.B., Pedersen, B.P. and Nissen, P. (2011) Crystal structure of a copper-transporting PIB-type ATPase. *Nature*, **475**, 59-64.

Gyobu, N., Tani, K., Hiroaki, Y., Kamegawa, A., Mitsuoka, K. and Fujiyoshi, Y. (2004) Improved specimen preparation for cryo-electron microscopy using a symmetric carbon sandwich technique. *J. Struct. Biol.*, **146**, 325-333.

Heitkamp, T., Kalinowski, R., Böttcher, B., Börsch, M., Altendorf, K. and Greie, J.C. (2008) K^+-translocating KdpFABC P-type ATPase from *Escherichia coli* acts as a functional and structural dimer. *Biochemistry*, **47**, 3564-3575.

Henderson, R. and Unwin, P.N.T. (1975) Three-dimensional model of purple membrane obtained by electron microscopy. *Nature*, **257**, 28-32.

Henderson, R., Baldwin, J., Downing, K., Lepault, J., Zemiln, F., 1986. Structure of purple membrane from *Halobacterium halobium*: recording, measurement and evaluation of electron micrographs at 3.5 Å resolution. *Ultramicroscopy* 19, 147-178.

Henderson, R., Baldwin, J.M., Ceska, T.A., Zemlin, F., Beckmann, E. and Downing, K.H. (1990) Model for the structure of bacteriorhodopsin based on high-resolution electron cryo-microscopy. *J. Mol. Biol.*, **213**, 899-929.

Henderson, R. (1992) Image contrast in high-resolution electron microscopy of biological macromolecules: TMV in ice. *Ultramicroscopy*, **46**, 1-18.

Henderson, R. and McMullan, G. (2013) Problem in obtaining perfect images by single-particle electron cryomicroscopy of biological structures in amorphous ice. *Microscopy (Tokyo)*, **62**, 43-50.

Hersey, S.J. and Sachs, G. (1995) Gastric acid secretion. *Physiol. Rev.*, **75**, 155–189.

Hirai, T., Murata, K., Mitsuoka, K., Kimura, Y. and Fujiyoshi, Y. (1999) Trehalose embedding technique for high-resolution electron crystallography: application to structural study on bacteriorhodopsin. *J. Electron. Microsc. (Tokyo)*, **48**, 653-658.

Hiroaki, Y., Tani, K., Kamegawa, A., Gyobu, N., Nishikawa, K., Suzuki, H., Walz, T., Sasaki, S., Mitsuoka, K., Kimura, K., Mizoguchi, A. and Fujiyoshi, Y. (2006) Implications of the aquaporin-4 structure on array formation and cell adhesion. *J. Mol. Biol.*, **355**, 628-639.

Ho, J.D., Yeh, R., Sandstrom, A., Chorny, I., Harries, W.E., Robbins, R.A., Miercke, L.J. and Stroud R.M. (2009) Crystal structure of human aquaporin 4 at 1.8 A and its mechanism of conductance. *Proc. Natl. Acad. Sci. USA.*, **106**, 7437-7442.

Hou, Z., Hu, Z., Blackwell, D.J., Miller, T.D., Thomas, D.D. and Robia, S.L. (2012) 2-Color calcium pump reveals closure of the cytoplasmic headpiece with calcium binding. *PLoS One*, **7**, 40369.

Jackson, R.J., Mendlein, J. and Sachs, G. (1983) Interaction of fluorescein isothiocyanate with the ($H^+ + K^+$)-ATPase. *Biochim. Biophys. Acta*, **731**, 9-15.

Jardetzky, O. (1966). Simple allosteric model for membrane pumps. *Nature*, **211**, 969-970.

Jensen, A.M., Sørensen, T.L., Olesen, C., Møller, J.V. and Nissen, P. (2006) Modulatory and catalytic modes of ATP binding by the calcium pump. *EMBO J.*, **25**, 2305-2314.

Jones, P.M. and George, A.M. (2000) Symmetry and structure in P-glycoprotein and ABC transporters what goes around comes around. *Eur. J. Biochem.*, **267**, 5298-5305

Jones., T.A., Zou, J.-Y., Cowan, S.W. and Kjeldgaard, M. (1991) Improved methods for building protein models in electron density maps and the location of errors in these models. *Acta. Crystallogr.*, **47**, 110–119.

Kanai, R., Ogawa, H., Vilsen, B., Cornelius, F. and Toyoshima, C. (2013) Crystal structure of a Na^+-bound Na^+,K^+-ATPase preceding the E1P state. *Nature*, **502**, 201-206.

Kimura,Y., Vassylyev, D.G., Miyazawa, A., Kidera, A., Matsushima, M., Mitsuoka, K., Murata, K., Hirai, T. and Fujiyoshi, Y. (1997) Surface of bacteriorhodopsin revealed by high-resolution electron crystallography. *Nature*, **389**, 206-211.

Klaassen, C.H.W. and De Pont, J.J.H.H.M. (1994) Gastric H^+/K^+-ATPase. *Cell Physiol. Biochem.*, **4**, 115–134.

Koning, R.I., Oostergetel, G.T. and Brisson, A. (2003) Preparation of flat carbon support films. *Ultramicroscopy*, **94**, 183-191.

Kühlbrandt, W., Wang, D.N. and Fujiyoshi, Y. (1994) Atomic model of plant light-harvesting complex by electron crystallography. *Nature*, **367**, 614-621.

Kühlbrandt, W. (2004). Biology, structure and mechanism of P-type ATPases. *Nat. Rev. Mol. Cell Biol.*, **5**, 282-295.

Liu, X., Daiho, T., Yamasaki, K., Wang, G., Danko, S. and Suzuki H. (2009) Roles of interaction between actuator and nucleotide binding domains of sarco(endo)plasmic reticulum Ca^{2+}-ATPase as revealed by single and swap mutational analyses of serine 186 and glutamate 439. *J. Biol. Chem.*, **284**, 25190-25198.

López-Marqués, R.L., Holthuis, J.C.M. and Pomorski, T.G. (2011) Pumping lipids with P4-ATPases. *Biol. Chem.*, **392**, 67–76.

Mitchell, P. (1957) A general theory of membrane transport from studies of bacteria. *Nature*, **180**, 134-136

Miyazawa, A., Fujiyoshi, Y. and Unwin, N. (2003) Structure and gating mechanism of the acetylcholine receptor pore. *Nature*, **423**, 949-955.

Møller, J.V., Juul, B. and le Maire, M. (1996) Structural organization, ion transport, and energy transduction of P-type ATPases. *Biochim. Biophys. Acta*, **1286**, 1-51.

Morth, J.P., Pedersen, B.P., Toustrup-Jensen, M.S., Sørensen, T.L., Petersen, J., Andersen, J.P., Vilsen, B. and Nissen, P. (2007) Crystal structure of the sodium-potassium pump. *Nature*, **450**, 1043-1049.

Morth, J.P., Pedersen, B.P., Buch-Pedersen, M.J., Andersen, J.P., Vilsen, B., Palmgren, M.G., Nissen, P. (2011) A structural overview of the plasma membrane Na^+,K^+-ATPase and H^+-ATPase ion pumps. *Nat. Rev. Mol. Cell Biol.*, **12**, 60-70.

Murata, K., Mitsuoka, K., Hirai, T., Walz, T., Agre, P., Heymann, J.B., Engel, A. and Fujiyoshi, Y. (2000) Structural determinants of water permeation through aquaporin-1. *Nature*, **407**, 599-605.

Munson, K., Vagin, O., Sachs, G. and Karlish S. (2003) Molecular modeling of SCH28080 binding to the gastric H,K-ATPase and MgATP interactions with SERCA- and Na,K-ATPases. *Ann. N. Y. Acad. Sci.*, **986**, 106–110.

Nishi, T. and Forgac, M. (2002) The vacuolar (H+)-ATPases--nature's most versatile proton pumps. *Nat. Rev. Mol. Cell Biol.*, **3**, 94-103

Nishizawa, T., Abe, K., Tani, K. and Fujiyoshi, Y. (2008) Structural analysis of 2D crystals of gastric H^+,K^+-ATPase in different states of the transport cycle. *J. Struct. Biol.*, **162**, 219-228.

Noble, J.E. and Bailey, M.J. (2009) Quantitation of protein. *Methods Enzymol.*, **463**, 73-95.

Ogawa, H., Stokes, D.L., Sasabe, H. and Toyoshima, C. (1998) Structure of the Ca^{2+} pump of sarcoplasmic reticulum: a view along the lipid bilayer at 9- Å resolution. *Biophys. J.*, **75**, 41-52.

Oshima, A., Tani, K., Hiroaki, Y., Fujiyoshi, Y. and Sosinsky, G.E. (2007) Three-dimensional structure of a human connexin26 gap junction channel reveals a plug in the vestibule. *Proc. Natl. Acad. Sci. USA.*, **104**, 10034-10039.

Palmgren, M. G. and Nissen, P. (2010). P-type ATPases. *Annu. Rev. Biophys.*, **40**, 243-266.

Pedersen, P. L. and Carafoli, E. (1987) Ion motive ATPases. I. Ubiquity, properties, and significance to cell function. *Trends Biochem. Sci.*, **12**, 146-150.

Pettersen, E.F., Goddard, T.D., Huang, C.C., Couch, G.S., Greenblatt, D.M., Meng, E.C. and Ferrin, T.E. (2004) UCSF Chimera--a visualization system for exploratory research and analysis. *J. Comput. Chem.*, **25**, 1605-1612.

Pedersen, B.P., Buch-Pedersen, M.J., Morth, J.P., Palmgren, M.G. and Nissen, P. (2007) Crystal structure of the plasma membrane proton pump. *Nature*, 450, 1111-1114.

Post, R.L. and Kume, S. (1973) Evidence for an aspartyl phosphate residue at the active site of sodium and potassium ion transport adenosine triphosphatase. *J. Biol. Chem.*, **248**, 6993-7000.

Puts, C.F. and Holthuis, J.C. (2009) Mechanism and significance of P4 ATPase-catalyzed lipid transport: lessons from a Na^+/K^+-pump. *Biochim. Biophys. Acta*, **1791**, 603-611

Rabon, E.C., McFall, T.L. and Sachs, G. (1982) The gastric [H,K]ATPase: H+/ATP stoichiometry. *J. Biol. Chem.*, **257**, 6296–6299.

Rabon, E,C, Bassilian, S., Sachs, G. and Karlish, S.J. (1990) Conformational transitions of the H,K-ATPase studied with sodium ions as surrogates for protons. *J. Biol. Chem.*, **265**, 19594-19599.

Rabon, E.C. and Reuben, M.A. (1990) The mechanism and structure of the gastric H,K-ATPase. *Annu. Rev. Physiol.*, **52**, 321–344.

Rabon, E., Sachs, G., Bassilian, S., Bassilian, S., Leach, C. and Keeling, D. (1991) A K^+-competitive fluorescent inhibitor of the H,K-ATPase. *J. Biol. Chem.*, **266**, 12395–12401.

Sachs, G., Shin, J.M., Vagin, O., Lambrecht, N., Yakubov, I. and Munson K. (2007) The gastric H,K ATPase as a drug target: past, present, and future. *J. Clin. Gastroenterol.*, **41**, 226-242.

Sali, A. and Blundell, T.L. (1993) Comparative protein modelling by satisfaction of spatial restraints. *J. Mol. Biol.*, **234**, 779-815.

Sawaguchi, A., Aoyama, F., Ide, S. and Suganuma, T. The cryofixation of isolated rat gastric mucosa provides new insights into the functional transformation of gastric parietal cells: an in vitro experimental model study. *Arch. Histol. Cytol.*, **68**, 151–160.

Sen, P.C. and Ray, T.K. (1979) Characterization of gastric mucosal membranes: lipid composition of purified gastric microsomes from pig, rabbit, and frog. *Arch Biochem Biophys.*, **198**, 548-555.

Shin, J.M., Munson, K., Vagin, O. and Sachs, G. (2009) The gastric HK-ATPase: structure, function, and inhibition. *Pflugers Arch.*, **457**, 609-622.

Shinoda, T., Ogawa, H., Cornelius, F. and Toyoshima, C. (2009) Crystal structure of the sodium-potassium pump at 2.4 Å resolution. *Nature*, **459**, 446-450.

Skou, J.C. (1957) The influence of some cations on an adenosine triphosphatase from peripheral nerves. *Biochim. Biophys. Acta*, **23**, 394-401.

Sørensen, D.M., Buch-Pedersen, M.J. and Palmgren, M.G. (2010) Structural divergence between the two subgroups of P5 ATPases. *Biochim. Biophys. Acta,* **1797**, 846-855.

Stewart, B., Wallmark, B. and Sachs, G. (1981) The interaction of H^+ and K^+ with the partial reactions of gastric ($H^+ + K^+$)-ATPase. *J. Biol. Chem.*, **256**, 2682–2690.

Suzuki, H., Ito, Y., Yamazaki, Y., Mineta, K., Uji, M., Abe, K., Tani, K., Fujiyoshi, Y. and Tsukita, S. (2013) The four-transmembrane protein IP39 of Euglena forms strands by a trimeric unit repeat. *Nat. Commun.*, **4**, 1766.

Sweadner, K.J. and Donnet, C. (2001) Structural similarities of Na,K-ATPase and SERCA, the Ca^{2+}-ATPase of the sarcoplasmic reticulum. *Biochem. J.*, **356**, 685–704.

Tani, K., Sasabe, H. and Toyoshima, C. (1996) A set of computer programs for determining defocus and astigmatism in electron images. *Ultramicroscopy*, **65**, 31-44.

Tani, K., Mitsuma, T., Hiroaki, Y., Kamegawa, A., Nishikawa, K., Tanimura, Y. and Fujiyoshi. Y. (2009) Mechanism of aquaporin-4's fast and highly selective water conduction and proton exclusion. *J. Mol. Biol.*, **389**, 694-706.

Toyoshima, C., Nakasako, M., Nomura, H. and Ogawa, H. (2000) Crystal structure of the calcium pump of sarcoplasmic reticulum at 2.6 A resolution. *Nature*, **405**, 647-655.

Toyoshima, C., Nomura, H., Tsuda, T. (2004) Lumenal gating mechanism revealed in calcium pump crystal structures with phosphate analogues. *Nature*, **432**, 361-368.

Toyoshima, C., Norimatsu, Y., Iwasawa, S., Tsuda, T. and Ogawa, H. (2007) How processing of aspartylphosphate is coupled to lumenal gating of the ion pathway in the calcium pump. *Proc. Natl. Acad. Sci. USA.*, **104**, 19831-19836.

Toyoshima, C. (2009) How Ca^{2+}-ATPase pumps ions across the sarcoplasmic reticulum membrane. *Biochim. Biophys. Acta*, **1793**, 941-946.

Tsai, C.J., Tani, K., Irie, K., Hiroaki, Y., Shimomura, T., McMillan, D.G., Cook, G.M., Schertler, G.F.X., Fujiyoshi, Y. and Li X.D. (2013). Two alternative conformations of a voltage-gated sodium channel. *J. Mol. Biol.*, **425**, 4074-4088.

Unwin, P.N.T. and Henderson, R. (1975) Molecular structure determination by electron microscopy of unstained crystalline specimens. *J. Mol. Biol.*, **94**, 425–440.

Unwin, P.N.T. and Fujiyoshi, Y. (2012) Gating movement of acetylcholine receptor caught by plunge-freezing. *J. Mol. Biol.*, **422**, 617-634.

Wallmark, B., Stewart, H.B., Rabon, E., Saccomani. G. and Sachs, G. (1980) The catalytic cycle of gastric (H+ + K+)-ATPase. *J. Biol. Chem.*, **255**, 5313–5319.

Walz, T. and Grigorieff, N. (1998) Electron Crystallography of Two-Dimensional Crystals of Membrane Proteins. *J. Struct. Biol.*, **121**, 142-161.

Widdas, W.F. (1952) Inability of diffusion to account for placental glucose transfer in the sheep and consideration of the kinetics of a possible carrier transfer. *J. Physiol.*, **118**, 23-39

Wolosin, J.M. (1985) Ion transport studies with H^+-K^+-ATPase-rich vesicles: implications for HCl secretion and parietal cell physiology. *Am. J. Physiol.*, **248**, 595–607.

Wriggers, W., Milligan, R.A., and McCammon, J.A. (1999) Situs: A package for docking crystal structures into low-resolution maps from electron microscopy. *J. Struct. Biol.*, **125**, 185–195.

Yang, F., Abe, K., Tani, K. and Fujiyoshi, Y. (2013). Carbon sandwich preparation preserves quality of two-dimensional crystals for cryo-electron microscopy. *Microscopy (Oxf)*, **62**, 597-606.

Yasuda, R., Noji, H., Kinoshita, K.Jr. and Yoshida, M. (1998) F1-ATPase is a highly efficient molecular motor that rotates with discrete 120º steps. *Cell*, **93**, 1117-1124

Yen, L.A., Cosgrove, P. and Holt, W. (1990) SDS purification of porcine H,K-ATPase from gastric mucosa. *Membr. Biochem.*, **9**, 129–140.